




Petrogenesis and tectonic implications of Early Paleozoic granitoids in the Qiaerlong district of the West Kunlun orogenic belt: constraints from petrology, geochronology, and Sr-Nd-Hf isotope geochemistry

Jinhong Xu , Zhengwei Zhang , Chengquan Wu , Xiyao Li , Ziru Jin , Pengcheng Hu , Taiyi Luo & Weiguang Zhu

To cite this article: Jinhong Xu , Zhengwei Zhang , Chengquan Wu , Xiyao Li , Ziru Jin , Pengcheng Hu , Taiyi Luo & Weiguang Zhu (2021): Petrogenesis and tectonic implications of Early Paleozoic granitoids in the Qiaerlong district of the West Kunlun orogenic belt: constraints from petrology, geochronology, and Sr-Nd-Hf isotope geochemistry, International Geology Review, DOI: [10.1080/00206814.2021.1882888](https://doi.org/10.1080/00206814.2021.1882888)

To link to this article: <https://doi.org/10.1080/00206814.2021.1882888>

 View supplementary material 

 Published online: 11 Feb 2021.

 Submit your article to this journal 

 Article views: 65

 View related articles 

 View Crossmark data 

ARTICLE



Petrogenesis and tectonic implications of Early Paleozoic granitoids in the Qiaerlong district of the West Kunlun orogenic belt: constraints from petrology, geochronology, and Sr-Nd-Hf isotope geochemistry

Jinhong Xu^{a,b}, Zhengwei Zhang^a, Chengquan Wu^a, Xiyao Li^{a,b}, Ziru Jin^{a,b}, Pengcheng Hu^{a,b}, Taiyi Luo^a and Weiguang Zhu^a

^aState Key Laboratory of Ore Deposit Geochemistry, Institute of Geochemistry, Chinese Academy of Sciences, Guiyang, China; ^bSchool of Earth and Planetary Sciences, University of Chinese Academy of Sciences, Beijing, China

ABSTRACT

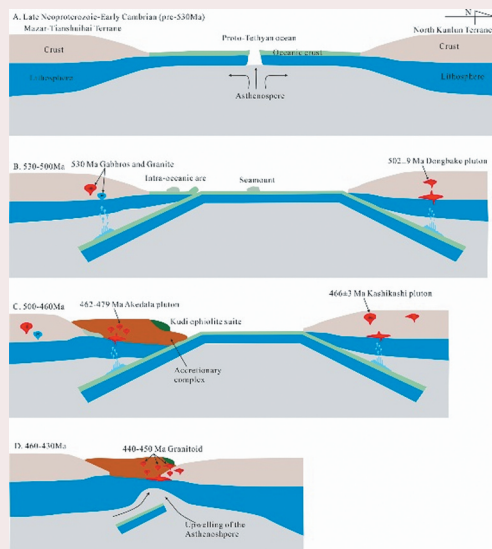
The West Kunlun orogenic belt (WKOB) is a complex orogenic belt that preserves the evidence of Early Palaeozoic and Late Palaeozoic orogenic events, with the former resulting from the closure of the Proto-Tethys Ocean. To better reveal the relationships between Early Palaeozoic granitoids in the WKOB and the tectonic evolution of the Proto-Tethys Ocean, we analysed the rocks of Akedala pluton, which is exposed within the Qiaerlong basin, and compared the results with contemporaneous magmatic rocks elsewhere in the WKOB. Integrated petrology, geochronology, and Sr–Nd–Hf isotope analyses of the rocks revealed the following: (1) The Akedala pluton is mainly composed of metaluminous–peraluminous I-type quartz monzonite and monzogranite; U–Pb dating of zircon indicates that quartz monzonite and monzogranite components is emplaced at 473–479 Ma and 462 Ma, respectively. (2) Both of them were enriched in large-ion lithophile elements and light rare earth elements and depleted in high field strength elements with negative Nb, Ta, Zr, P and Ti anomalies, indicating that they formed in a subduction zone environment. (3) Quartz monzonites were enriched in MgO concentrations (>3.10 wt.%), and show variable whole rock Sr–Nd isotopic ratios ($^{87}\text{Sr}/^{86}\text{Sr}_i = 0.7042\text{--}0.7058$, $\epsilon_{\text{Nd}}(t) = -0.4$ to $+1.1$), and had positive zircon $\epsilon_{\text{Hf}}(t)$ (+0.0 to $+6.8$) values, which suggests they are derived from a mixed source of juvenile crust and older lower crust. (4) Monzogranites were characterized by high Sr (461–804 ppm) and low Y (2.00–3.68 ppm) and Yb (0.19–0.31 ppm) contents with high Sr/Y (164–325) and (La/Yb)_N (12.6–46.7) ratios, indicating an adakitic affinity; they had relatively homogeneous whole rock ($^{87}\text{Sr}/^{86}\text{Sr}_i$; 0.7044–0.7045) and positive $\epsilon_{\text{Nd}}(t)$ (+2.0 to $+2.9$) and positive zircon $\epsilon_{\text{Hf}}(t)$ (+1.1 to $+4.3$) values with low MgO, Cr, Ni and Nb contents, suggesting that they were mainly generated from partial melting of thickened lower crust. Comparative analysis of these results with other Early Palaeozoic arc magmas in the WKOB shows that the Akedala pluton was formed due to the southward subduction of the Proto-Tethys Ocean. Divergent bidirectional subduction of the Proto-Tethys Ocean was initiated in the Early Cambrian, continued through the Middle Ordovician, and ended in the Early Silurian, due to terminal collision between the Tarim block and the West Kunlun terrane, which created the Early Palaeozoic orogenic belt.





ARTICLE HISTORY

Received 8 July 2020
Accepted 26 January 2021

KEYWORDS

Arc magmatism; akedala granitoid; west Kunlun orogen; proto-Tethys Ocean



CONTACT Zhengwei Zhang  zhangzhengwei@vip.gyig.ac.cn  State Key Laboratory of Ore Deposit Geochemistry, Institute of Geochemistry, Chinese Academy of Sciences, Guiyang 550018, China.; Chengquan Wu  wuchengquan@mail.gyig.ac.cn
 Supplemental data for this article can be accessed here.

© 2021 Informa UK Limited, trading as Taylor & Francis Group

1. Introduction

The West Kunlun orogenic belt (WKOB) is located in the western part of the central China orogenic belt (CCOB) (Figure 1A–B), bordering the Tarim Basin in the north and the Tibetan Plateau in the south. WKOB experienced subduction–accretion–collision of the Proto- and Paleo-Tethys Oceans during the Early Palaeozoic and the Late Palaeozoic, respectively, and thus, it is a complex orogenic belt preserving the evidence of both the Early Palaeozoic and the Late Palaeozoic deformational events (Figure 1C; Pan 2000; Zhang *et al.* 2019a, b). The Proto-Tethys Ocean was subducted and closed along the Oyttag-Kudi-Qimanyut suture zone during the Early Palaeozoic, forming the orogenic belt that contains ophiolite mélanges, accretionary wedges, arc granitoids, and high-Ba/Sr granites (Figure 1C and Table 1; Xiao *et al.* 2002; Zhang *et al.* 2019a). Many studies have revealed that the arc granitoids were emplaced in the Cambrian (Hu *et al.* 2016; Zhu *et al.* 2018; Zhang *et al.* 2018a; Li *et al.* 2019; Liu *et al.* 2019; Yin *et al.* 2020), the Early–Middle Ordovician (Xiao *et al.* 2002, 2005; Yuan *et al.* 2002; Liao *et al.* 2010; Liu *et al.* 2014; Li *et al.* 2019), and the Late Ordovician (Zhang *et al.* 2007b; Ye *et al.* 2008). The sources of the arc magmas have been proposed as ancient crust (Zhang *et al.* 2019d), subducted sediments (Liao *et al.* 2010), enriched lithospheric mantle (Hu *et al.* 2016; Liu *et al.* 2019), and a mantle wedge (Zhang *et al.* 2018a). In addition, many researchers have suggested that these granites formed either due to southward subduction (Jiang *et al.* 2002; Liao *et al.* 2010; Jia *et al.* 2013; Liu *et al.* 2014; Li *et al.* 2019; Zhang *et al.* 2018a, 2019), northward subduction (Xiao *et al.* 2000; Wang 2004; Ye *et al.* 2008), or bidirectional subduction (Xiao *et al.* 2002, 2005; Zhu *et al.* 2018). Although comprehensive previous research and published data can be used to analyse the relationship between tectonic and magmatic events in the WKOB, many issues remain unresolved, including how the subduction–collision process and petrogenesis of arc granitoids are related to the tectonic evolution of the Proto-Tethys Ocean.

Studies have shown that the northern belt of the WKOB is characterized by back-arc basin extension and the related Cu–Pb–Zn–Mn mineralization of the Late Palaeozoic age (Zhang *et al.* 2006, 2014, 2019e; Jiang *et al.* 2008; Ji *et al.* 2018). However, there are only few magmatic rocks related to the Proto-Tethys Ocean in the north WKOB. Recently, it has been recognized that the Akedala (AK) pluton, which occurs within the Qiaerlong basin, has geological features similar to the Early Palaeozoic granitoids in the southern part of the WKOB (Figure 1C). Therefore, it has been speculated that it may

represent a valuable record of magmatism related to the subduction of the Proto-Tethys Ocean in the northern belt of the WKOB.

In this study, we present new and comprehensive field observations, petrography, laser ablation inductively coupled plasma mass spectrometry (LA–ICP–MS), zircon U–Pb geochronology, whole-rock major and trace element data, and Sr–Nd–Hf isotope ratios from the AK pluton to constrain the crystallization ages and explore the petrogenesis of its granitoid components. These data are then combined with the results of previous studies conducted on Early Palaeozoic granites in the WKOB to better understand the evolution of the Proto-Tethys Ocean in this area.

2. Geological setting

The WKOB has been tectono-stratigraphically subdivided into four tectonic units separated by three suture zones. From north to south, these comprise the North Kunlun terrane (NKT), the Oyttag-Kudi-Qimanyute suture (OKQS), the South Kunlun terrane (SKT), the Mazha-Kangxiwa-Subashi suture zone (MKSS), the Mazar-Tianshuihai terrane (MTT), the Hongshanhu-Qiaoertianshan suture (HQS), and the Karakorum terrane (KKT) (Figure 1C; Pan 2000; Zhang *et al.* 2019a).

The NKT, also termed the Tiekeliike belt or the southern margin of the Tarim Basin (Pan 2000), is an uplifted terrane that represents the basement of the Tarim Basin. The crystalline basement is composed of the Paleoproterozoic Heluositan complex and the 2.41 Ga Akazi pluton. The basement experienced amphibolite- to granulite-facies metamorphism at 1.9 Ga (Zhang *et al.* 2007a), and it is unconformably covered by the Neoproterozoic Sailajiazitage Group volcanic-sedimentary sequence and the Ailiankate Group clastic rocks (Zhang *et al.* 2016a).

The SKT is mainly composed of volcano-sedimentary sequences belonging to the Saitula Group and the Bulunkuole Group, which were deposited during the Late Neoproterozoic to Cambrian and are unconformably covered by Upper Palaeozoic to Mesozoic volcanic rocks (Pan 2000; Zhang *et al.* 2018b). Recent studies have shown that the SKT is a large accretionary wedge that formed via the southward subduction of the Proto-Tethys Ocean during the Early Palaeozoic (Yuan *et al.* 2002; Zhang *et al.* 2019a). The accretionary wedge includes a fore-arc complex, seamount, arc volcano-sedimentary sequence, and ophiolite, which were all metamorphosed to amphibolite facies conditions at 440 Ma (Yuan *et al.* 2002; Zhang *et al.* 2019a, b).

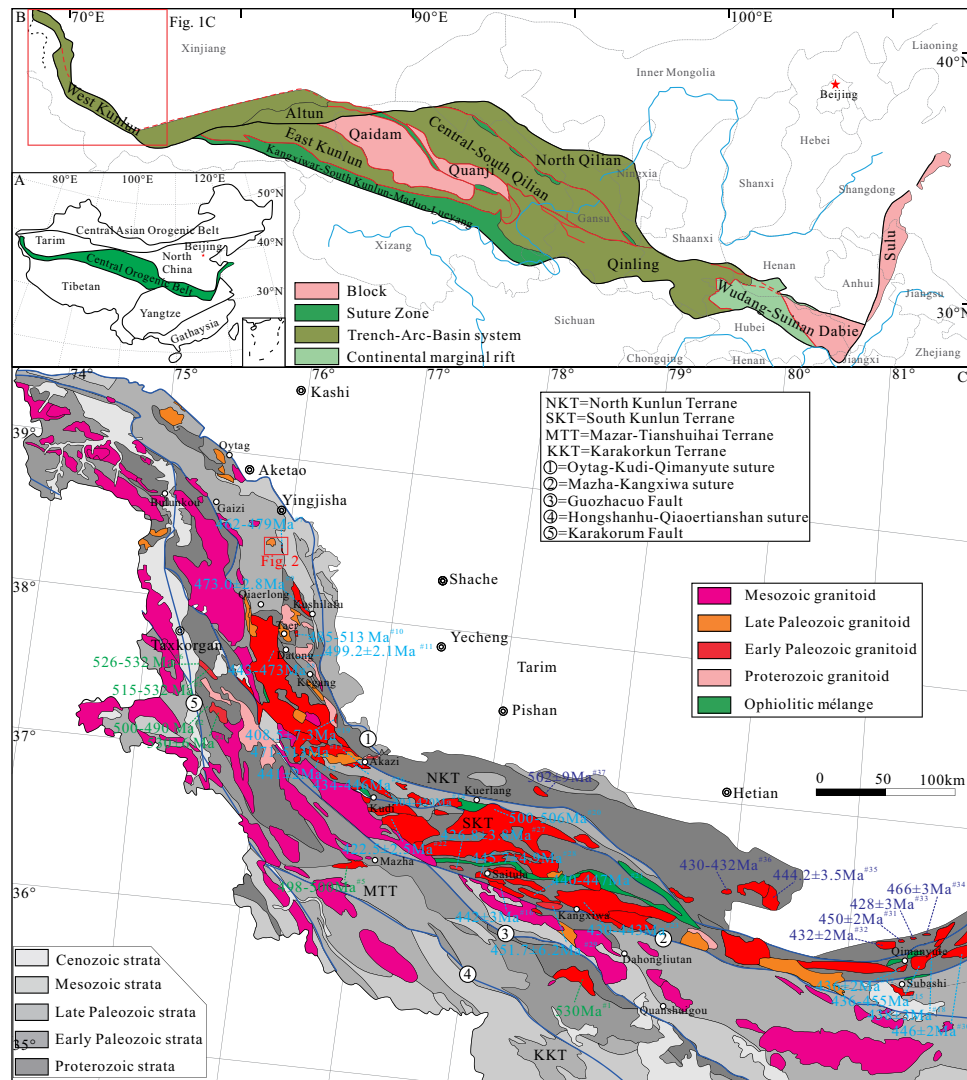


Figure 1. A. Schematic map showing the tectonic units of China. B. Schematic map showing the central China orogenic belt (CCO). C. Simplified geological map of the West Kunlun orogenic belt (WKOB) (modified after Pan 2000; Zhang *et al.* 2019a, b). Zircon U–Pb ages are also labelled and summarized in Table 1

The MTT is mainly composed of crystalline basement rocks of the Mazar Complex (Zhang *et al.* 2019b) and is covered by the Tianshuihai Group (Zhang *et al.* 2018c). The basement comprises bimodal volcanic rocks and sedimentary sequences that were deposited at 2.5 Ga, and it underwent amphibolite-facies metamorphism at 2.0 Ga (Ji *et al.* 2011; Zhang *et al.* 2018b). The cover is a Late Palaeozoic passive continental margin sedimentary sequence intruded by Cambrian gabbro and Mesozoic granite (Hu *et al.* 2016; Zhang *et al.* 2018c).

The KKT is mainly composed of Proterozoic crystalline schist, gneiss, quartzite, and marble, and Cambrian phyllite, schist, and limestone of the Heihezi Group; it is covered by a Palaeozoic clastic-carbonate sedimentary sequence (Pan 2000).

The WKOB was assembled during the subduction-driven closure of the Proto- and Paleo-Tethys Oceans and contains voluminous magmatic rocks that developed as two large, parallel, and NW–SE-trending I-type magmatic suites over 1000 km in length. These occur between the OKQS and MKS, and between the Late Palaeozoic–Early Mesozoic belt in the south and the Late Mesoproterozoic–Early Palaeozoic belt in the north (Figure 1C; Pan 2000; Xiao *et al.* 2002). The southern magmatic rocks that are related to the tectonic evolution of the Paleo-Tethys Ocean occur mainly along the southern part of the SKT and the northern margin of the MTT. The northern magmatic suites consist of Precambrian magmatic rocks, early Palaeozoic plutons, and ophiolitic mélanges (Xiao *et al.* 2002). The Precambrian magmatic rocks are mainly composed of

Table 1. Summary of geochronological data for Early Palaeozoic plutons in the WKOB.

Terrane	Pluton No.	Rock type	Mineral	Age		References
				Method	Mean Age (Ma)	
Tianshuihai T.	1. Nanpingxueshan	Medium-grained porphyritic biotite-quartz monzonite	Zircon	LA-ICP-MS	484.5 ± 2.7	Hu <i>et al.</i> 2016, Hu <i>et al.</i> 2017a
		Medium-fined grained biotite-quartz monzonite	Zircon	LA-ICP-MS	527.9 ± 2.8	Hu <i>et al.</i> 2016, Hu <i>et al.</i> 2017a
		Metagabbro	Zircon	LA-ICP-MS	532.3 ± 3.1	Hu <i>et al.</i> 2016, Hu <i>et al.</i> 2017a
		Dolerite	Zircon	LA-MC-ICP-MS	498.6 ± 4.2	Liu <i>et al.</i> 2019
		Granite	Zircon	LA-MC-ICP-MS	524.8 ± 2.2	Liu <i>et al.</i> 2019
		Granite	Zircon	LA-MC-ICP-MS	532.7 ± 2.5	Liu <i>et al.</i> 2019
		Monzonite	Zircon	LA-ICP-MS	530.9 ± 3.0	Yin <i>et al.</i> 2020
		Gabbro	Zircon	SHRIMP	491.4 ± 2.5	Liu <i>et al.</i> 2019
		Biotite monzonitic granite gneisses	Zircon	LA-ICP-MS	515 ± 2	Zhu <i>et al.</i> 2016
		Monzonite	Zircon	LA-ICP-MS	532.8 ± 3.7	Yin <i>et al.</i> 2020
		Granitic porphyry	Zircon	LA-ICP-MS	530 ± 6	Zhu <i>et al.</i> 2016
		Granite	Zircon	LA-ICP-MS	500.7 ± 1.1	Zhang <i>et al.</i> 2016b
			Zircon	LA-ICP-MS	498.7 ± 1.4	Zhang <i>et al.</i> 2016b
			Zircon	SHRIMP	529.9 ± 2.8	Zhang <i>et al.</i> 2018a
			Zircon	SHRIMP	526 ± 3	Zhang <i>et al.</i> 2018a
		Southern Kunlun T.	7. Akedala	Gabbro	Zircon	SHRIMP
Gabbro	Zircon			SHRIMP	473 ± 2	This study
Meta-rhyolite	Zircon			LA-ICP-MS	479 ± 2	This study
Monzonite	Zircon			LA-ICP-MS	462 ± 2	This study
Granite	Zircon			LA-ICP-MS	459 ± 3	This study
Quartz monzonite	Zircon			LA-ICP-MS	452 ± 5	Zhu <i>et al.</i> 2018
Monzogranite	Zircon			LA-ICP-MS	447.7 ± 5.2	Liao <i>et al.</i> 2010
Host granitoid	Zircon			SHRIMP	469.3 ± 5.3	Liao <i>et al.</i> 2010
Host granitoid	Zircon			SHRIMP	453.5 ± 6.0	Liao <i>et al.</i> 2010
Host granitoid	Zircon			SHRIMP	465.3 ± 4.8	Liao <i>et al.</i> 2010
Host granitoid	Zircon			SHRIMP	473.4 ± 5.3	Liao <i>et al.</i> 2010
Quenched enclave	Zircon			SHRIMP	448.0 ± 4.6	Liao <i>et al.</i> 2010
Dark-Coloured porphyritic syenite and monzonite	Zircon			LA-MC-ICP-MS	434 ± 0.9	Wang <i>et al.</i> 2017
Dark-Coloured porphyritic syenite and monzonite	Zircon			LA-MC-ICP-MS	444 ± 0.9	Wang <i>et al.</i> 2017
Light-Coloured adakitic dykes of granite and monzonite	Zircon			LA-MC-ICP-MS	443.6 ± 1.4	Wang <i>et al.</i> 2017
Light-Coloured adakitic dykes of granite and monzonite	Zircon			LA-MC-ICP-MS	462.0 ± 1.0	Wang <i>et al.</i> 2017
Monzogranites and quartz diorites	Zircon	SHRIMP	457 ± 7	Li <i>et al.</i> 2019		
Monzogranite	Zircon	SHRIMP	478 ± 5	Li <i>et al.</i> 2019		
Porphyritic granites	Zircon	SHRIMP	490 ± 4	Li <i>et al.</i> 2019		
Monzonite	Zircon	LA-ICP-MS	513.1 ± 2.1	Yin <i>et al.</i> 2020		
Gabbros and serpentized peridotites.	Zircon	SHRIMP	490 ± 5	Li <i>et al.</i> 2019		
Monzogranite	Zircon	LA-ICP-MS	441 ± 2	Wang <i>et al.</i> 2013		
Quartz monzodiorite	Zircon	Single-grain	471 ± 5	Yuan <i>et al.</i> 2002		
	Zircon	SHRIMP	513 ± 7	Liu <i>et al.</i> 2014		
Diorite	Zircon	LA-ICP-MS	513.7 ± 2.1	Yin <i>et al.</i> 2020		
Granodiorite	Zircon	Single-grain	405 ± 2	Yuan <i>et al.</i> 2002		
Syenogranite	Zircon	SHRIMP	420.6 ± 6.3	Liu <i>et al.</i> 2014		
Biotite granite	Zircon	SHRIMP	408 ± 7	Xiao <i>et al.</i> 2005		
Two-mica granitoids	Zircon	Single-grain	404	Yuan <i>et al.</i> 2002		
Gabbros	Zircon	LA-MC-ICP-MS	455 ± 2	Zhang <i>et al.</i> 2019c		
Biotite granite	Zircon	LA-MC-ICP-MS	436 ± 2	Zhang <i>et al.</i> 2019c		
	Zircon	LA-ICP-MS	442 ± 3	Zhang <i>et al.</i> 2019d		

(Continued)

Table 1. (Continued).

Terrane	Pluton No.	Rock type	Age			References	
			Mineral	Method	Mean Age (Ma)		
Northern Kunlun T.	17. Akesaiyin	Granodiorite	Zircon	LA-ICP-MS	436 ± 2	Zhang <i>et al.</i> 2019d	
	18. South Qimanyute	Biotite granite	Zircon	LA-ICP-MS	438 ± 3	Zhang <i>et al.</i> 2019d	
	19. Duweituiwei	Dolerite	Zircon	LA-ICP-MS	408.5 ± 7.3	Liu <i>et al.</i> 2016	
	20. Kuerliang	Medium-grained porphyritic granodiorite	Zircon	Single-grain SHRIMP	500.2 ± 1.2	Zhang <i>et al.</i> 2007b	
	21. Menggubao	Hornblende diorite and tonalite	Zircon	SHRIMP	506 ± 9.8	Zhang <i>et al.</i> 2007b	
	22. Sugaitelike	Granite	Zircon	LA-ICP-MS	440.5 ± 4.6	Cui <i>et al.</i> 2006	
	23. Tamaerte	Medium coarse-grained hornblende biotite monzogranite	Zircon	SHRIMP	422.5 ± 2.5	Zhuan <i>et al.</i> 2018	
	24. Akaz	Medium-grained biotite monzogranite	Zircon	SHRIMP	443.1 ± 2.3	Cui <i>et al.</i> 2007a	
				Zircon	SHRIMP	430.7 ± 2.6	Cui <i>et al.</i> 2007a
				Zircon	LA-ICP-MS	411.3 ± 1.4	Zheng <i>et al.</i> 2013
				Zircon	LA-ICP-MS	449.6 ± 0.68	Zheng <i>et al.</i> 2013
				Zircon	LA-ICP-MS	449.8 ± 1.8	Zheng <i>et al.</i> 2013
				Zircon	LA-ICP-MS	499.3 ± 2.5	Zheng <i>et al.</i> 2013
	25. Buziwan	Quartz monzodiorite	Zircon	SHRIMP	403 ± 7	Xiao <i>et al.</i> 2005	
	26. Qiukesu	Tonalite	Zircon	SHRIMP	434.7 ± 7.8	Jia <i>et al.</i> 2013	
		Quartz monzodiorite	Zircon	SHRIMP	446.9 ± 7.0	Jia <i>et al.</i> 2013	
		monzogranite and syenogranite	Zircon	LA-ICP-MS	426 ± 3.8	Zhang <i>et al.</i> 2016c	
		Intermediate enclave	Zircon	LA-ICP-MS	445 ± 4.9	Zhang <i>et al.</i> 2016c	
	27. West Saitula	Host	Zircon	LA-ICP-MS	445 ± 2.9	Zhang <i>et al.</i> 2016c	
	28. Saitula	MME	Zircon	LA-ICP-MS	451.7 ± 6.2	Zhang <i>et al.</i> 2016c	
	29. West Kangxiwa	Quartz diorite	Zircon	SIMS	446 ± 3	Zhang <i>et al.</i> 2016d	
	30. Alamas	Biotite granite	Zircon	LA-ICP-MS	450 ± 2	Zhang <i>et al.</i> 2019d	
	31. Alaleike	Granodiorite	Zircon	LA-ICP-MS	432 ± 2	Zhang <i>et al.</i> 2019d	
	32. Yamen	Monzogranite	Zircon	LA-ICP-MS	428 ± 3	Zhang <i>et al.</i> 2019d	
	33. Kuidaimai	Fine grained granodiorite	Zircon	LA-MC-ICP-MS	466 ± 2	Zhang <i>et al.</i> 2019c	
	34. Kashikashi	Granodiorite	Zircon	LA-ICP-MS	444.2 ± 3.5	Hu 2018	
	35. Tiekelike	High Ba–Sr granite	Zircon	SHRIMP	430 ± 12	Ye <i>et al.</i> 2008	
	36. Buya	Host monzodiorite	Zircon	LA-MC-ICP-MS	432.6 ± 2.5	Hu <i>et al.</i> 2017b	
		Enclave	Zircon	LA-MC-ICP-MS	432.4 ± 6.4	Hu <i>et al.</i> 2017b	
	37. Dongbake	Gneissic tonalite	Zircon	SHRIMP	502 ± 9	Cui <i>et al.</i> 2007b	

the Paleoproterozoic Heluositan complex, the Paleoproterozoic Akazi pluton, and the Mesoproterozoic Azibaileidi pluton (Zhang *et al.* 2007a; Ye *et al.* 2016). Early Palaeozoic magmatism related to the tectonic evolution of the Proto-Tethys Ocean comprises abundant mafic to felsic granitoids that were emplaced along the NKT, SKT, and TST, including the Cambrian–Ordovician I-type arc granites and Silurian high-Ba/Sr and A-type granites (Figure 1C and Table 1; Jiang *et al.* 2002; Yuan *et al.* 2002; Xiao *et al.* 2005; Yuan *et al.* 2005; Cui *et al.* 2007a, b; Zhang *et al.* 2007b; Ye *et al.* 2008; Liao *et al.* 2010; Liu *et al.* 2014; Hu *et al.* 2016; Wang *et al.* 2017; Zhang *et al.* 2018a; Zhu *et al.* 2018; Li *et al.* 2019; Liu *et al.* 2019; Zhang *et al.* 2019a, b, d; Yin *et al.* 2020).

3. Sampling and analytical methods

3.1 Sampling

The AK pluton occurs in the Qiaerlong basin; it has an exposed area of 12 km², and is surrounded by the Early Jurassic Kangsu and Late Carboniferous–Early Permian Tegeinaiqikedaban Formations (Figure 2). It is mainly composed of a medium-grained grey–green lithology and a fine-grained grey lithology (Figure 3). Both of lithologies are typically dominated by K-feldspar, plagioclase, and quartz, although the actual proportions of each mineral vary between them (Figure 3). The former contains plagioclase (35–45 vol.%), alkali feldspar (25–35 vol.%), quartz (10–20 vol.%), amphibole (10–15 vol.%), and pyroxene (1–5 vol.%), which plot in the quartz

monzonite field on a Quartz–Alkaline feldspar–Plagioclase–Feldspathoid (QAPF) diagram (Figure 4). And the later contains plagioclase (35–40 vol.%), alkali feldspar (20–35 vol.%), quartz (30–45 vol.%), and mica (<1 vol.%), which plot in the monzogranite field on a QAPF diagram (Figure 4). Plagioclase is often surrounded by K-feldspar, which is a typical monzonitic texture, and quartz is interstitial to feldspar. The accessory minerals in the granitoids include zircon, apatite, titanite, and magnetite (Figure 3). Weak, late-stage hydrothermal alteration is represented by the epidotization of feldspar.

Ten representative samples were collected from the AK pluton along an N–S transect, four of which were quartz monzonites and six were monzogranites (Figure 2). The geochemical analyses of these samples included zircon U–Pb age dating, whole-rock major and trace element geochemistry, and Sr–Nd–Hf isotope analysis, which were conducted simultaneously by LA-ICP-MS at the State Key Laboratory of Ore Deposit Geochemistry, Institute of Geochemistry, Chinese Academy of Sciences.

3.2 Analytical methods

After removing the rims and weathered portions of the sampled hand specimens, each sample was individually crushed and ground to a fine powder for bulk-rock chemical analysis. Three representative samples (~5 kg) were used for zircon U–Pb dating of the AK pluton: two quartz monzonites (AKDL-2 and AKDL-4) and one monzogranite (AKDL-8). Zircon grains were separated from each sample using traditional heavy liquid and magnetic

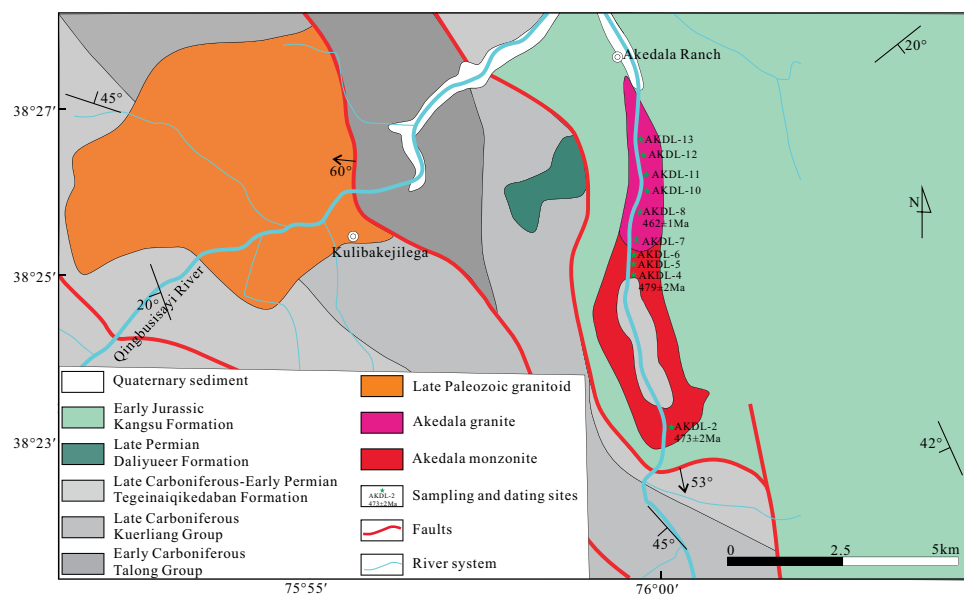


Figure 2. Geological map of the Akedala pluton with sampling and dating sites shown (modified after Henan Institute of Geological Survey 2005).

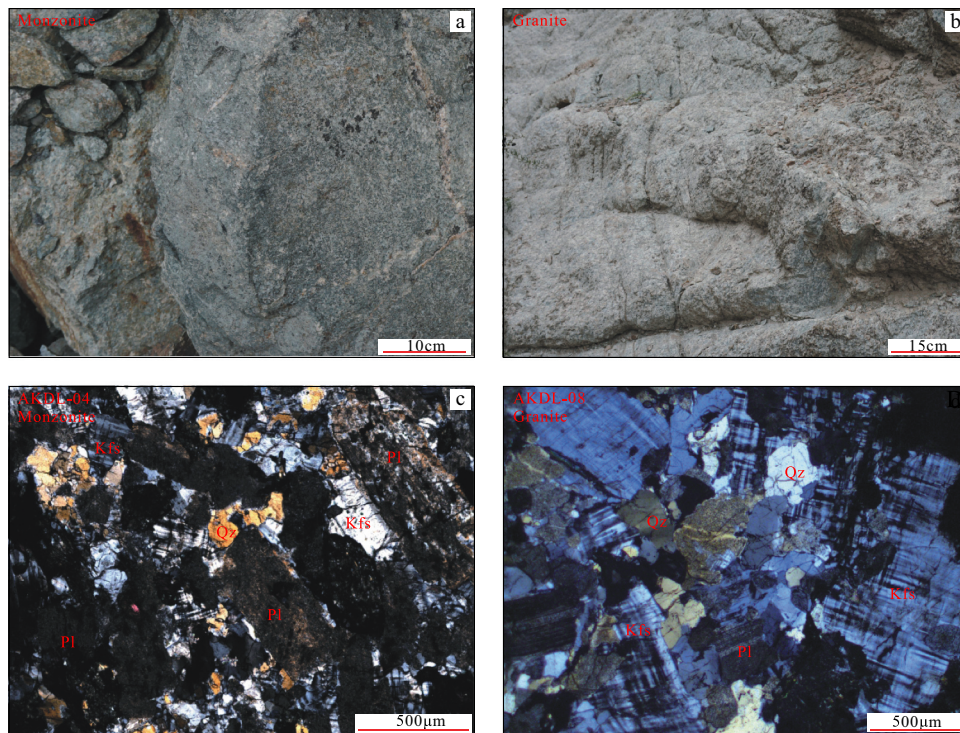


Figure 3. A–B. Photographs of representative lithologies from the AK pluton. C–D. Major mineral assemblages and typical textures in the AK pluton.

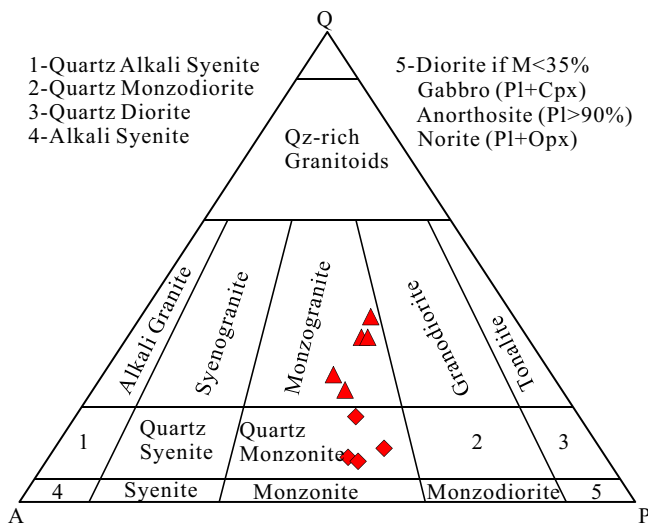


Figure 4. QAPF classification of the AK pluton (modified from Streckeisen 1967).

separation techniques, after which they were hand-picked under a binocular microscope and mounted in epoxy resin. The epoxy mounts were then polished down to near-half sections of the grains to reveal their internal structures for cathodoluminescence (CL) imaging, U–Pb dating, and Hf isotopic analyses.

Sample powders (~0.4 g) were accurately weighed and then fluxed with 4 g of $\text{Li}_2\text{B}_4\text{O}_7$ at 1150–1200°C in preparation of homogeneous glass disks used for X-ray fluorescence (XRF) analyses. The major element concentrations were determined using an ARL Perform' X 4200 Sequential X-Ray Fluorescence Spectrometer (Thermo Fisher Scientific Inc.), which has an analytical precision better than 1 wt.%.

Trace element analyses were performed following the procedures described by Qi *et al.* (2000), which required ~50 mg of sample powder to be accurately weighed and dissolved by a HF + HNO_3 solution in high-pressure Teflon bombs for two days at 190°C. Rhenium was chosen as an internal standard to monitor the signal drift during counting. The trace element contents were analysed using a Perkin-Elmer SCIEX ELAN DRC-e ICP–MS, which has a precision better than 10% (Qi *et al.* 2000).

Sample preparation for whole-rock Sr–Nd isotope analyses were performed by weighing, spiking, and dissolving ~100–150 mg of sample powders with 15 mL of a HF + HNO_3 + HClO_4 solution in Teflon bombs for seven days at 200°C. The isotope solution was subsequently separated using conventional cation-exchange techniques, and the ratios were analysed using a Neptune plus multi-collector inductively coupled plasma mass spectrometer (MC-ICP–MS).

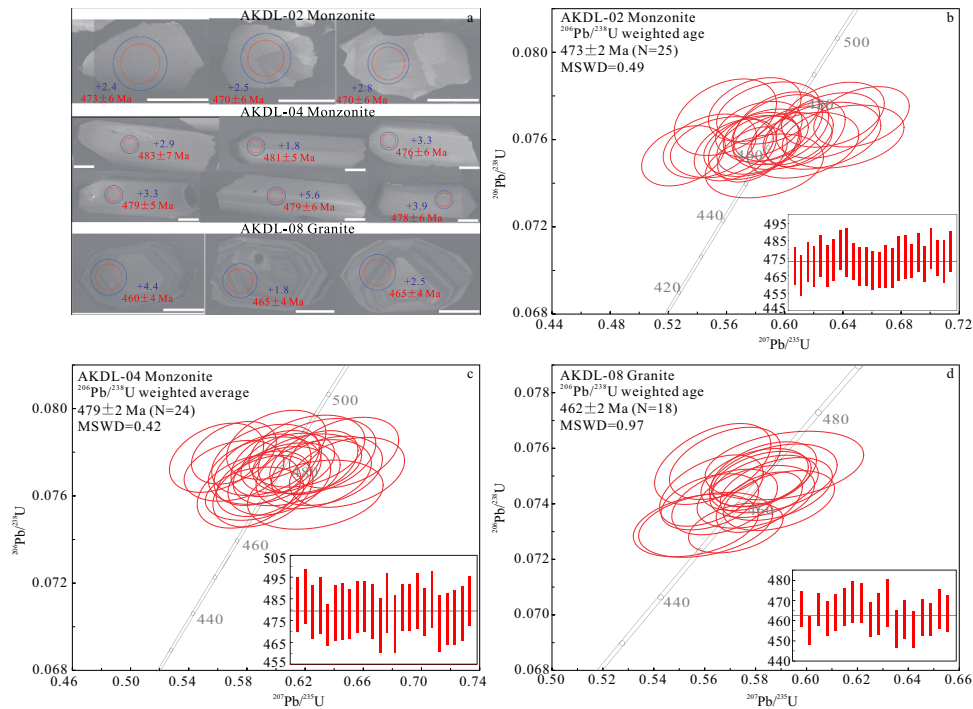


Figure 5. A. Representative cathodoluminescence (CL) images of zircon from quartz monzonite and monzogranite from the AK pluton. Solid red and purple circles show the location of LA-ICP-MS U–Pb analyses and LA-MC-ICP-MS Hf analyses, respectively. The scale bar in all CL images is 50 μm in length. U–Pb concordia diagrams for quartz monzonite (B–C) and monzogranite (D) components.

Zircon trace element analyses and U–Pb dating were performed with LA-ICP-MS using a GeoLas Pro 193 nm ArF excimer laser. An Agilent 7500x ICP-MS was used to acquire ion-signal intensities using a beam diameter of 32 μm , repetition time of 6 Hz, and energy density of 5 J/cm². Helium was used as a carrier gas. Each analysis involved a background measurement of 20 s (gas blank) followed by 40 s of data acquisition and an additional 20 s of wash time. Offline data processing was conducted using ICPMSDataCal (Liu *et al.* 2008, 2010). Zircon 91,500 was selected as the external standard for U–Pb dating and was analysed twice after every 10 analyses (i.e. two zircon 91,500 standards, 10 samples, two zircon 91,500 standards etc.). Uncertainties of the preferred values for the external standard 91,500 were propagated through calculations used to determine the ages for each sample. Concordia plots and weighted mean ages were calculated using the Isoplot (Ludwig 2003). Trace element contents of zircons were measured against multiple reference materials (NIST 610, BHVO-2 G, BCR-2 G, and BIR-1 G) and integrated with Si internal standardization.

Zircon Lu–Hf isotope analyses were performed using a RESOLUTION S-155 laser ablation system (ASI, Australia) connected to a Nu Plasma III MC-ICP-MS (Nu Instruments, Wrexham, UK) with a beam diameter of 44 μm , repetition time of 6 Hz, and energy density of

64 J/cm². Helium was used as the carrier gas at an uptake rate of 280 mL/min. Each analysis incorporated a background acquisition of 20 s followed by 40 s of ablation for signal collection. The isobaric interferences of ¹⁷⁶Lu and ¹⁷⁶Yb on ¹⁷⁶Hf were calibrated by counting ¹⁷⁵Lu and ¹⁷³Yb and using the ratios of ¹⁷⁶Lu/¹⁷⁵Lu = 0.02658 and ¹⁷⁶Yb/¹⁷³Yb = 0.796218. Mass fractionation of Yb and Hf isotope ratios was corrected by normalizing to ¹⁷²Yb/¹⁷³Yb = 1.35274 and ¹⁷⁹Hf/¹⁷⁷Hf = 0.7325, respectively, using an exponential law.

4. Analytical results

4.1. Zircon LA-ICP-MS U–Pb dating

Zircons separated from the sample AKDL-2 are 50–200 μm long with length-to-width ratios between 1:1 and 2:1, colourless to light brown, subhedral to euhedral in shape, and have cores that are either banded or homogenous, surrounded by rims with weak oscillatory zoning in CL images (Figure 5A). All 25 analytical spots produced broadly concordant ²⁰⁶Pb/²³⁸U and ²⁰⁷Pb/²³⁵U ages that match each other within analytical errors. These analyses showed variable abundances of U (72.5–208 ppm) and Th (34.1–128 ppm), producing Th/U ratios of 0.4–0.8 (Supplementary Table 1). The 25

analyses produced a weighted mean $^{206}\text{Pb}/^{238}\text{U}$ age of 473 ± 2 Ma (MSWD = 0.49, 2σ) (Figure 5B), which is identical, within error, to the concordant age of 473 ± 2 Ma (MSWD = 0.45, 2σ).

Zircons separated from the sample AKDL-4 are 100–250 μm long with length-to-width ratios between 2:1 and 3:1, colourless to light brown, euhedral in shape, and have homogenous cores surrounded by rims with weak oscillatory zoning in CL images (Figure 5A). All 24 analytical spots showed variable abundances of U (67.7 to 136 ppm) and Th (32.7 to 108 ppm), producing Th/U ratios of 0.4 to 0.9 (Supplementary Table 1). All 24 analyses yielded a weighted mean $^{206}\text{Pb}/^{238}\text{U}$ age of 479 ± 2 Ma (MSWD = 0.42, 2σ) (Figure 5C), which is identical, within error, to the concordant age of 479 ± 1 Ma (MSWD = 0.10, 2σ).

Zircons separated from the sample AKDL-8 are 100–200 μm long with length-to-width ratios between 1:1 and 2:1, colourless to light brown, euhedral in shape, and have clear zonation textures in CL images (Figure 5A). All 18 analytical spots showed variable abundances of U (137 to 551 ppm) and Th (49.8 to 423 ppm), producing Th/U ratios of 0.4 to 1.0 (Supplementary Table 1). All 18 analyses yielded a weighted mean $^{206}\text{Pb}/^{238}\text{U}$ age of 462 ± 2 Ma (MSWD = 0.97, 2σ) (Figure 5D), which is identical, within error, to the concordant age of 462 ± 1 Ma (MSWD = 0.49, 2σ).

4.2. Major and trace elements

Major and trace element data of all samples for the AK pluton are listed in Supplementary Table 2. The quartz monzonites contain moderate SiO_2 contents (55.29–56.84 wt.%) and are alkalis-enriched ($\text{K}_2\text{O} + \text{Na}_2\text{O} = 6.75\text{--}7.16$ wt. %), such that they plot in the monzonite field on a total alkali vs. silica diagram and along the alkaline to the calc-alkaline series (Figure 6A). The quartz

monzonites are enriched in TiO_2 (0.75–1.06 wt.%), Al_2O_3 (15.28–18.08 wt.%), $\text{Fe}_2\text{O}_3^{\text{T}}$ (7.24–8.89 wt.%), MnO (0.12–0.15 wt.%), MgO (3.10–4.70 wt.%), CaO (1.68–5.11 wt.%), K_2O (3.57–4.69 wt.%), and P_2O_5 (0.19–0.29 wt.%) (Supplementary Table 2). They are peraluminous with A/CNK (molecular ratio of $\text{Al}_2\text{O}_3/[\text{CaO} + \text{Na}_2\text{O} + \text{K}_2\text{O}]$) and A/NK (molecular ratio of $\text{Al}_2\text{O}_3/[\text{Na}_2\text{O} + \text{K}_2\text{O}]$) values of 0.83–1.41 and 1.69–1.97 (Figure 6B), respectively. In contrast, the analysed monzogranites have significantly higher SiO_2 (68.29–71.70 wt. %) and alkalis contents ($\text{K}_2\text{O} + \text{Na}_2\text{O} = 7.37\text{--}8.90$ wt. %), such that they plot along the calc-alkaline series on a total alkali vs. silica diagram (Figure 6A). The monzogranites have A/CNK and A/NK ratios of 0.87–1.11 and 1.91–2.82, respectively, indicating that they are metaluminous to peraluminous (Figure 6B). The monzogranites have relatively low TiO_2 , Al_2O_3 , $\text{Fe}_2\text{O}_3^{\text{T}}$, MnO, MgO, CaO, K_2O , and P_2O_5 contents (Supplementary Table 2), and form a continuous trend with the quartz monzonites (Figure 7).

The AK pluton quartz monzonites have total rare earth element (REE) contents of 90.25–113.76 ppm. Chondrite-normalized REE patterns of the quartz monzonites invariably show relative enrichment of light rare earth elements (LREE) with $(\text{La}/\text{Yb})_{\text{N}}$ ratios of 4.43–9.57 and weak negative Eu anomalies ($\delta\text{Eu} = 0.84\text{--}0.90$) (Figure 8A). The monzogranites have lower total REE contents than the quartz monzonites (19.52–60.44 ppm) and show weakly positive to negative Eu anomalies ($\delta\text{Eu} = 0.95\text{--}1.28$) (Figure 8A). In primitive mantle (PM)-normalized multi-element diagrams, the quartz monzonites and monzogranites are depleted in Nb, Ta, P, and Ti, and enriched in K, Pb, Sr, and LREE (Figure 8B).

4.3. Sr and Nd isotopic results

Whole-rock Rb–Sr and Sm–Nd isotopic compositions of the AK pluton are listed in Supplementary Table 3 and shown in Fig. 9. All initial $^{87}\text{Sr}/^{86}\text{Sr}$ isotopic ratios ($^{87}\text{Sr}/^{86}\text{Sr}$

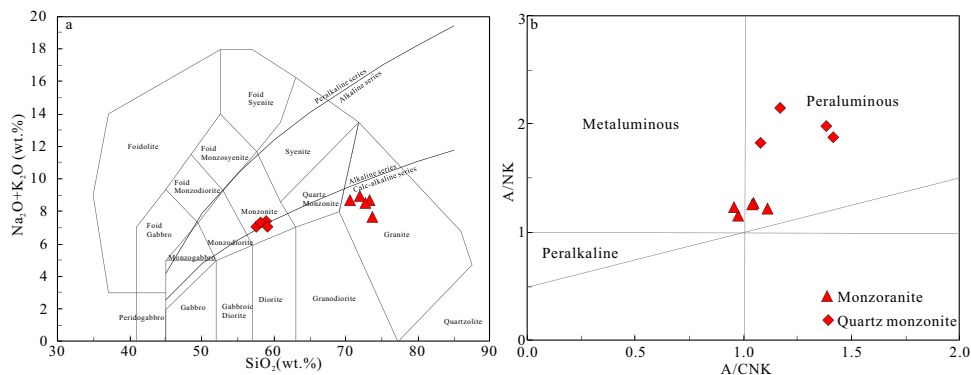


Figure 6. A. Plot of $(\text{Na}_2\text{O} + \text{K}_2\text{O})$ vs. SiO_2 (modified from Middlemost 1994). B. Plot of A/NK [molar ratio of $\text{Al}_2\text{O}_3/(\text{Na}_2\text{O} + \text{K}_2\text{O})$] vs. A/CNK [molar ratio of $\text{Al}_2\text{O}_3/(\text{CaO} + \text{Na}_2\text{O} + \text{K}_2\text{O})$] (modified from Maniar and Piccoli 1989) for the AK pluton.

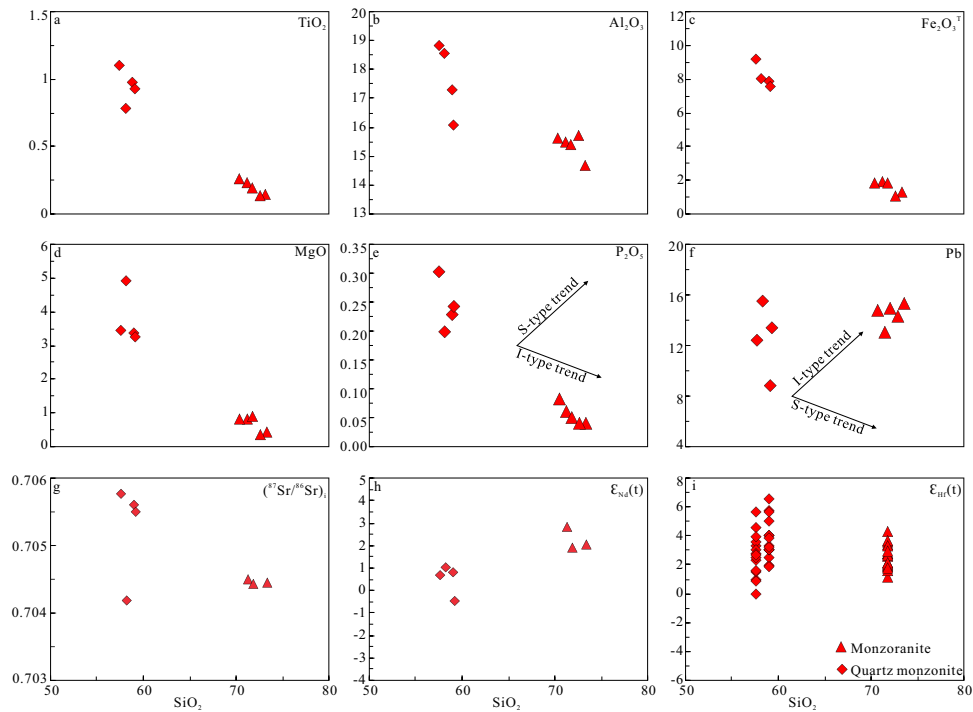


Figure 7. Selected major and trace elements and Sr–Nd–Hf isotope vs. SiO_2 diagrams for the AK pluton. A. TiO_2 . B. Al_2O_3 . C. $\text{Fe}_2\text{O}_3^{\text{T}}$. D. MgO. E. P_2O_5 . F. Pb. G. $(^{87}\text{Sr}/^{86}\text{Sr})_i$. H. $\epsilon_{\text{Nd}}(t)$. I. $\epsilon_{\text{Hf}}(t)$.

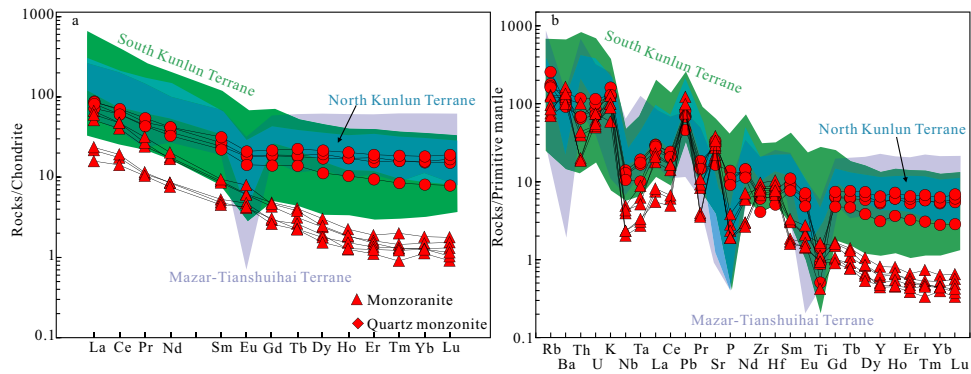


Figure 8. A. Chondrite-normalized REE patterns for the AK pluton. B. Primitive Mantle (PM)-normalized trace element patterns for the AK pluton. Chondrite and PM values are from Sun and McDonough (1989)

Sr_i and $\epsilon_{\text{Nd}}(t)$ values were calculated according to the weighted mean $^{206}\text{Pb}/^{238}\text{U}$ ages for each monzonite and granite sample. The quartz monzonites have moderate Sr contents (350–710 ppm) and high Rb contents (104–165 ppm), and these show a variable initial $^{87}\text{Sr}/^{86}\text{Sr}$ of 0.704187–0.705772. They have high Sm contents (3.38–4.83 ppm), high Nd contents (15.3–19.6 ppm), and variable $\epsilon_{\text{Nd}}(t)$ values (–0.4 to +1.1), which produce two-stage Nd model ages of 1.12–1.24 Ga. In contrast, the monzogranites have moderate Sr (461–604 ppm) and low Rb contents (61.0–81.6 ppm), and these show homogeneous initial $^{87}\text{Sr}/^{86}\text{Sr}$ ratios of 0.704432–0.704500. They have low Sm contents (0.811–1.38 ppm), low Nd

contents (4.04–8.29 ppm), relatively homogeneous $\epsilon_{\text{Nd}}(t)$ values (+2.0 to +2.9), and therefore, similar two-stage Nd model ages of 0.96–1.04 Ga.

4.4. Hf isotope compositions of zircon

In situ Lu–Hf isotopic compositions of zircons from the AK pluton were analysed in the same spots used for U–Pb age determination by LA-ICP-MS, and all initial $^{176}\text{Hf}/^{177}\text{Hf}$ ratios and $\epsilon_{\text{Hf}}(t)$ values were back-calculated to their weighted mean $^{206}\text{Pb}/^{238}\text{U}$ age. The results are listed in Supplementary Table 4 and are shown in Figure 10. Zircons from quartz monzonite and monzogranite

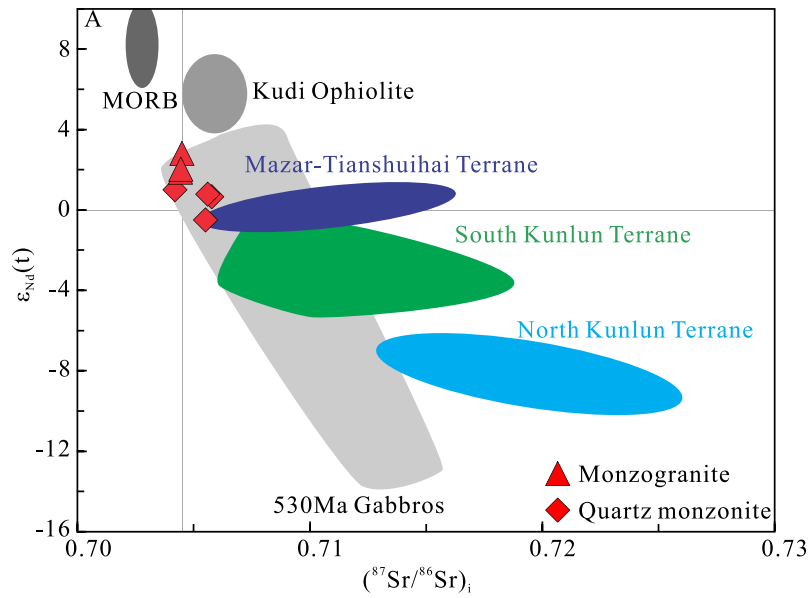


Figure 9. $(^{87}\text{Sr}/^{86}\text{Sr})_i$ vs. $\epsilon_{\text{Nd}}(t)$ plot for the AK pluton. Data sources are as follows: mid-ocean ridge basalt (MORB) (Chauvel and Blichert-Toft 2001), Kudi ophiolite (Pan 2000), Precambrian metaigneous and metasedimentary rocks in SKT (Jia *et al.* 2013), and Early Palaeozoic arc granitoids in the WKOB (references are shown in Table 1).

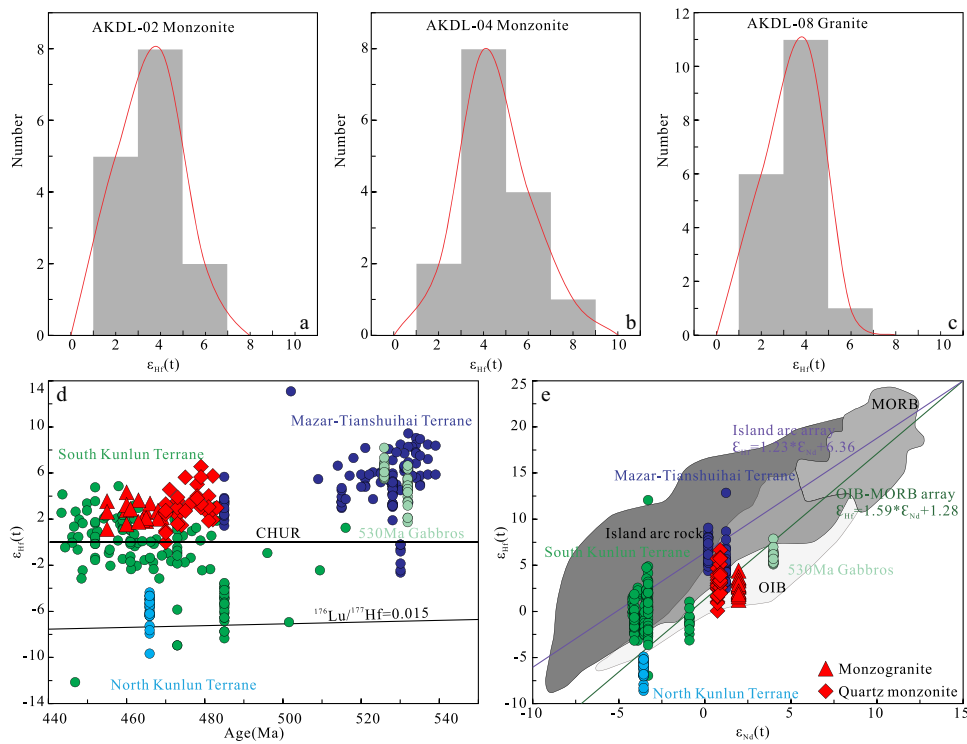


Figure 10. Histograms of zircon $\epsilon_{\text{Hf}}(t)$ values for quartz monzonite (A–B), and monzogranite (C) from the AK pluton, $\epsilon_{\text{Hf}}(t)$ values vs. zircon U–Pb ages from the AK pluton (D), and $\epsilon_{\text{Hf}}(t)$ values vs. $\epsilon_{\text{Nd}}(t)$ values from the AK pluton (Chauvel *et al.* 2008, 2009). The Early Palaeozoic arc granitoids in the WKOB are the same as shown in Figure 8

within the AK pluton all have similar positive $\epsilon_{\text{Hf}}(t)$ values. Sample AKDL-2 (473 ± 2 Ma) has $\epsilon_{\text{Hf}}(t)$ values of +0.0 to +5.6, with a major peak at $\epsilon_{\text{Hf}}(t) = +4$, and two-stage Hf model ages of 0.96–1.22 Ga (Figure 10A).

Sample AKDL-4 (479 ± 2 Ma) has $\epsilon_{\text{Hf}}(t)$ values of +1.9 to +6.6, with a major peak at $\epsilon_{\text{Hf}}(t) = +4$, and two-stage Hf model ages of 0.96–1.22 Ga (Figure 10B). Sample AKDL-8 (462 ± 2 Ma) has $\epsilon_{\text{Hf}}(t)$ values of +1.1 to +4.3, with

a major peak at $\epsilon_{\text{Hf}}(t) = +4$, and two-stage Hf model ages of 1.07–1.25 Ga (Figure 10C).

5. Discussion

5.1 Genetic types

Granitoids are generally divided into S-, I-, and A-types (Collins et al., 1982; Whalen et al., 1987). The A/CNK values of quartz monzonites were higher than 1.1, indicating that their peraluminous compositions are in agreement with felsic S-type granites (Figure 6B; Chappell and White 1992). Quartz monzonites mainly contained plagioclase, K-feldspar, and quartz (Figure 3A, C), and no peraluminous minerals were found in of this study. They had low Zr (46.0–78.8 ppm), low Nb (7.52–9.96 ppm), low (Zr + Nb + Ce + Y) (105–161 ppm) contents, and low $10,000 \times \text{Ga}/\text{Al}$ ratios (2.05–2.22) that are distinct from those of A-type granites ($\text{Zr} \geq 250$ ppm, $\text{Nb} \geq 20$ ppm, $(\text{Zr} + \text{Nb} + \text{Ce} + \text{Y}) \geq 350$ ppm, and $10,000 \times \text{Ga}/\text{Al} \geq 2.6$; Whalen et al., 1987). Quartz monzonites showed a negative relationship between P_2O_5 and SiO_2 (Figure 7E), and a positive relationship between Pb and SiO_2 (Figure 7F). This is consistent with the trend observed for I-type granites (Chappell and White 1992; Wu et al. 2003).

Monzogranites had high SiO_2 contents (68.29–71.70 wt.%) and low A/CNK values (0.96–1.11), with a similar mineral assemblage (Figure 3B, D) and geochemical trend (Figure 7E, F) to quartz monzonites, also indicative of I-type granite affinity. They were enriched in Sr (461–804 ppm), have low Y (2.00–3.68 ppm) and Yb (0.19–0.31 ppm) contents with high Sr/Y (164–325) and $(\text{La}/\text{Yb})_{\text{N}}$ (12.6–46.7) ratios that are similar to those of adakite ($\text{Sr} \geq 400$ ppm, $\text{Y} \leq 18$ ppm, $\text{Yb} \leq 1.8$ ppm, $\text{Sr}/\text{Y} \geq 20$ and $(\text{La}/\text{Yb})_{\text{N}} \geq 10$; Figure 11A, B; Martin 1999). In addition, they had low MgO and Nb contents and high SiO_2 contents that show geochemical affinities to high- SiO_2 adakitic rocks (Figure 11C–D; Martin et al. 2005).

5.2 Petrogenesis

The AK quartz monzonites had relatively low SiO_2 (57.60–59.17 wt.%) and high MgO contents (3.27–4.92 wt.%) and bulk Mg number ($\text{Mg}^{\#} = \text{Mg}/(\text{Mg} + \text{Fe}^{2+})$) of 42–55 that were consistent with those of the partial melts from mafic crust (Rudnick and Gao 2003). In addition, they had a wide range of Nb/Ta (12.9–18.6), Nb/U (3.25–6.90) and Ce/Pb (2.81–4.24) ratios, with average values of 14.4, 4.97 and 3.26, similar to those of continental crust (11.4, 6.15, and 3.91; Rudnick and Gao 2003), further suggesting a crustal origin.

However, quartz monzonites show a large variations in depleted whole rock Sr–Nd isotopic ratios ($^{87}\text{Sr}/^{86}\text{Sr}$;

$= 0.7042\text{--}0.7058$, $\epsilon_{\text{Nd}}(t) = -0.4$ to $+1.1$; Fig. 9), indicating that they were derived from a mixed magma. The zircon $\epsilon_{\text{Hf}}(t)$ values also varied ($+0.0$ to $+6.8$) with almost seven ϵ_{Hf} units (Fig. 9D). This is consistent with an open-system magma chamber where mantle-derived basaltic melt may be mixed with crustal components (Griffin et al. 2002), thereby producing the observed isotopic variability in the AK quartz monzonites. The two-staged Nd model ages (1.11–1.24 Ga, Supplementary Table 3) and two-stage Hf model ages (0.96–1.32 Ga, Supplementary Table 4) of quartz monzonites were significantly younger than the crystallization age of the basement metamorphic rocks of the Tarim Basin (the Paleoproterozoic Heluositan complex and the 2.41 Ga Akazi pluton; Zhang et al. 2007a) and the MTT (the 2.5 Ga Mazar complex; Ji et al. 2011; Zhang et al. 2018b), suggesting that the quartz monzonites were originated from a Mesoproterozoic source. The studied rocks had positive zircon $\epsilon_{\text{Hf}}(t)$ values ($+0.0$ to $+6.8$), and plotted above the evolutionary trend defined by the lower crust and near the chondritic uniform reservoir (CHUR) reference line in $t\text{--}\epsilon_{\text{Hf}}(t)$ diagram (Figure 10D), which suggests that a mixed source of a juvenile crust and an older lower crust was involved in the origin of quartz monzonites.

As mentioned above, the AK monzogranites show adakitic affinities. Several petrogenetic models have been proposed to explain the origins of adakites, including: (1) melting of subducted young oceanic crust (Defant and Drummond 1990); (2) fractional crystallization of water-rich arc magma (Macpherson et al. 2006; Richards and Kerrich 2007); (3) magma mixing between felsic and basaltic magmas (Streck et al. 2007); and (4) partial melting of thickened lower crust (Chung et al. 2003; Zhu et al. 2009).

Monzogranites were high- SiO_2 adakitic rocks with a high SiO_2 (68.29–71.70 wt.%), and low MgO (0.34–0.87 wt.%), Nb (1.65–3.46 ppm), Cr (9.88–18.9 ppm) and Ni (1.74–6.13 ppm) contents (Figure 11C–F), which were distinct from the adakites that were derived from subducted young oceanic crust; they were generally similar to high-Mg andesites with high MgO, Nb, Cr, and Ni contents (Defant and Drummond 1990; Rapp et al. 1999; Martin et al. 2005).

Adakites can be formed by garnet fractional crystallization under high pressure and plagioclase and amphibole fractional crystallization under low pressure (Macpherson et al. 2006; Richards and Kerrich 2007). Both formation mechanisms have an important impact on the chondrite-normalized REE patterns; for example, garnet crystallization influences HREE and Y contents, plagioclase fractional crystallization affects Eu and Sr values, while amphibole fractional crystallization affects middle REE (MREE) concentrations. However, monzogranites

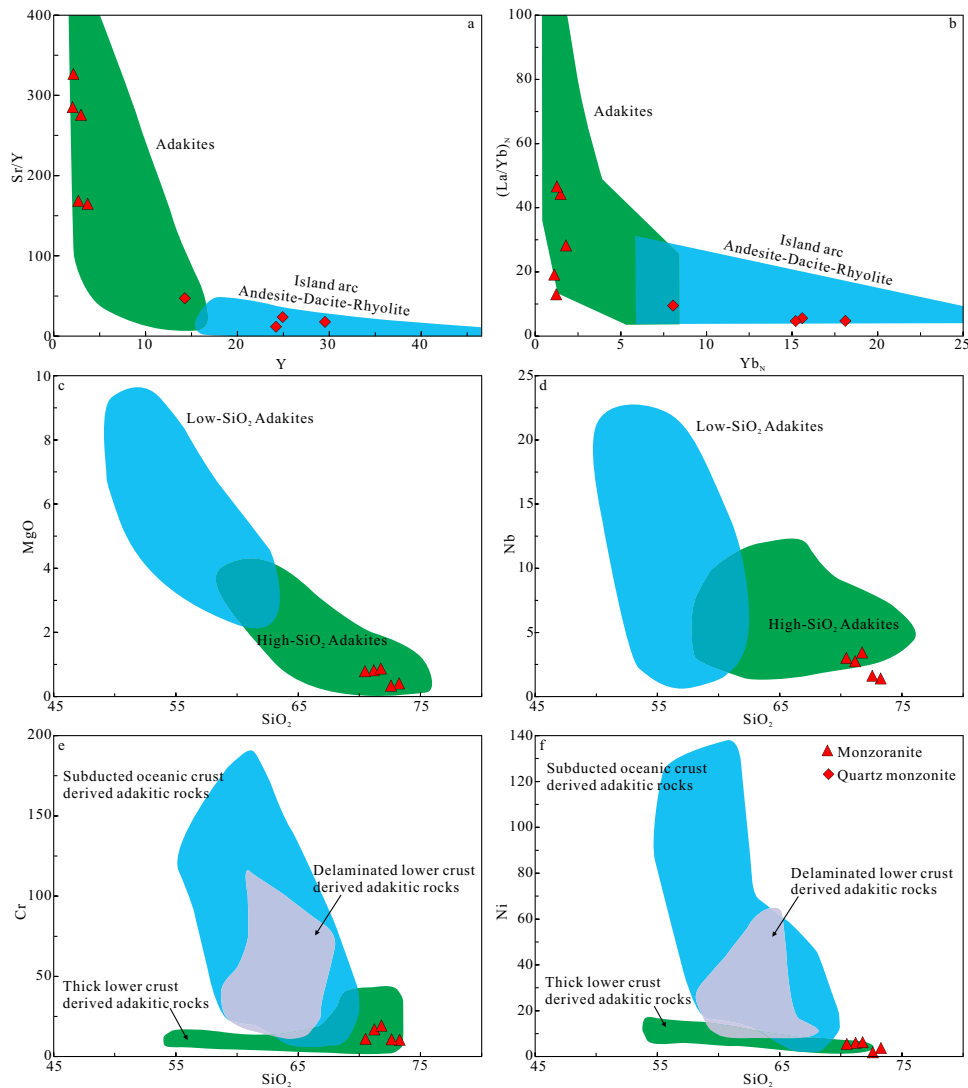


Figure 11. (A) Sr/Y versus Y; (B) $(La/Yb)_N$ versus $(Dy/Yb)_N$ (after Martin 1999); (C) MgO versus SiO_2 ; (D) Nb versus SiO_2 (after Martin *et al.* 2005); (E) Cr versus SiO_2 ; (F) Ni versus SiO_2 (after Wang *et al.* 2006).

show flat chondrite-normalized REE patterns without any significant negative Eu anomalies (Figure 8A), indicating that neither of these formation mechanisms played an important role in the generation of the AK monzogranites. In addition, there were no significant linear trends in the Sr/Y, $(La/Yb)_N$, Eu^* versus SiO_2 diagrams (Figure 12A–C), or in the $(Dy/Yb)_N$ versus $(La/Yb)_N$ diagram (Figure 12D), and no significant negative Sr anomalies in PM normalized trace element patterns (Figure 8B), further suggesting that fractional crystallization was not responsible for the petrogenesis of the AK monzogranites.

Monzogranites had similar Sr–Nd–Hf isotopic data to quartz monzonites in the AK pluton, however, it is unlikely that monzogranites can be a result of fractional crystallization of quartz monzonites. Zircons from quartz monzonites show relatively homogeneous CL characteristics with weak oscillatory zoning in rim domains, while

monzogranites show clear zonation textures (Figure 5A), which suggests that zircons formed in different magma systems. Geochronological data revealed a gap of at least 10 Ma between quartz monzonites and monzogranites, suggesting that they were from two independent magmatic systems, an early one with intermediate composition (479 ± 2 Ma and 473 ± 2 Ma for monzonites) and a later one with felsic composition (462 ± 2 Ma for granite) (Figure 5C–D). A distinct compositional gap in SiO_2 concentrations between monzogranites (68.29–71.70 wt.%) and quartz monzonites (55.29–56.84 wt.%) is inconsistent with a fractional model in which the SiO_2 concentrations gradually increased (Bellieni *et al.*, 1986; Garland *et al.* 1995). In addition, more evolved magmas are enriched in $Na_2O + K_2O$ along with fractional crystallization, which contrasts with the fact that $Na_2O + K_2O$ decrease with the increasing SiO_2 content (Figure 6A).

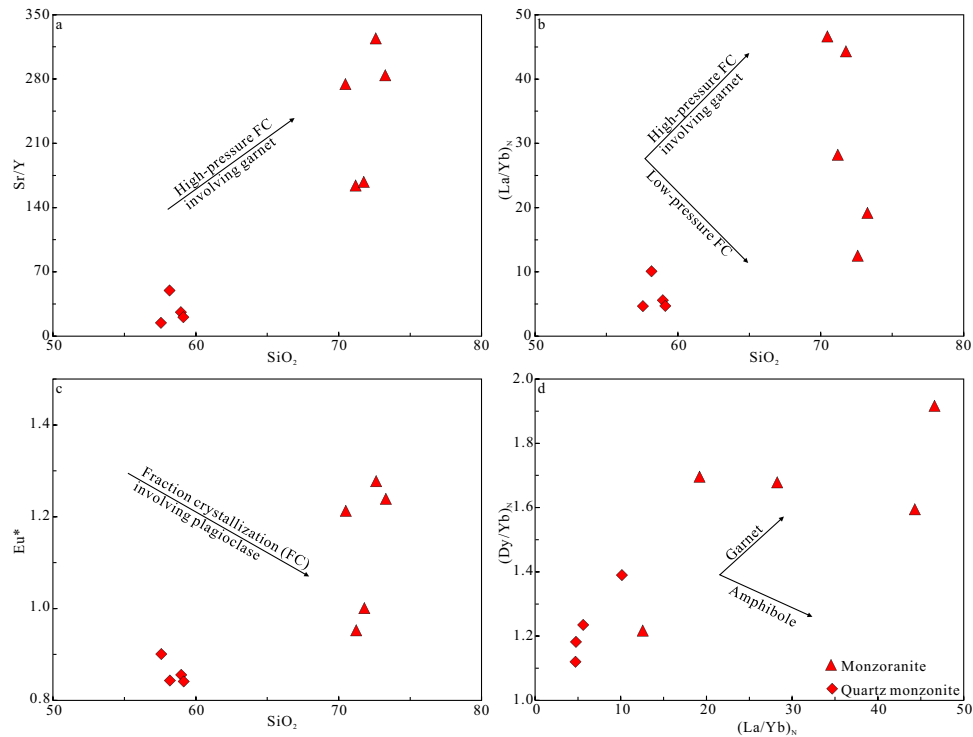


Figure 12. (A) Sr/Y versus SiO₂; (B) (La/Yb)_N versus SiO₂; (C) Eu* versus SiO₂; (D) (Dy/Yb)_N versus (La/Yb)_N. High-pressure fractional crystallization involving garnet and amphibole are cited from Macpherson *et al.* (2006). Fractional crystallization involving plagioclase are cited from Wang *et al.* (2006)

Therefore, the mineralogical and geochemical differences further suggest that fractional crystallization of quartz monzonites was not responsible for the origin of the adakitic monzogranites.

Monzogranites have high SiO₂ and low Cr and Ni contents that plotted in thick lower crust-derived adakitic rocks (Figure 11E, F; Martin *et al.* 2005), suggesting that the adakites were likely generated by partial melting of the thickened lower crust. They have low MgO contents and low Mg# values (38–48), which were similar to experimental melts of meta-basalt and eclogite under 1–4.0 GPa (Figure 13A; Rapp and Watson 1995; Rapp *et al.* 1999). Monzogranites have low K₂O/Na₂O (0.45–0.76) and CaO/Al₂O₃ (0.04–0.13) ratios, which are consistent with those of lower crustal-derived adakites, but are different from those of oceanic slab melts (Figure 13B; Stern and Kilian, 1996; Karsli *et al.* 2019). They have Nb/Ta ratios (9.85–14.9) with average values (12.3) intermediate between the mantle (17.7; Sun and McDonough 1989) and the lower crust (8.3; Rudnick and Gao 2003), indicating that monzogranites were probably generated by the partial melting of amphibole and hornblende eclogite in the garnet stability field (Figure 13C; Foley *et al.* 2002). In addition, the studied adakitic monzogranites had moderate to high La/Yb (17.5–65.1), La/Sm (5.44–12.0) and Sm/Yb (3.22–6.59) ratios with average values of 42.2, 8.50, and 4.73, respectively, similar to

those of melts sourced from the lower crust at depths of 45–50 km with garnet-bearing eclogite residues (La/Yb > 30 and Sm/Yb > 5; Rapp *et al.* 1999). This is also consistent with the 513-Ma-old thick lower crust-derived Yierba adakitic diorite (41.6, 10.1, and 4.13; Yin *et al.* 2020) in the plot of La/Sm versus Sm/Yb (Figure 13D; Haschke *et al.* 2006), and this indicates that monzogranites were generated from a thickened lower crust. Furthermore, the AK adakitic monzogranites had higher Sm/Yb ratios than quartz monzonites (Figure 13D), indicating that monzogranites were formed under relatively higher pressures. Finally, monzogranites have a relatively homogeneous whole rock (⁸⁷Sr/⁸⁶Sr)_i (0.7044–0.7045) and ε_{Nd}(t) (+2.0 to +2.9) values zircon ε_{Hf}(t) values (+1.1 to +4.3) and show older two-staged Nd-Hf model ages (0.97–1.25 Ga) (Supplementary Tables 3 and 4), suggesting that monzogranites were mainly derived from partial melting of a thickened lower crust.

Monzonites and monzogranites of the AK pluton underwent crystallization fractionation, as indicated by their variable major and trace elements. The TiO₂, Fe₂O₃^T, and MgO contents were negatively correlated with the SiO₂ content (Figure 7A–C), which reflects the fractionation of mafic minerals (i.e. pyroxene and hornblende). They show negative Ba, Sr, P, and Ti anomalies in the PM normalized trace elements (Figure 8B), indicating plagioclase, apatite and Fe-Ti oxide fractionation. The Ba

contents of monzonites and monzogranites are negatively correlated with their Rb contents, but positively correlated with their Sr contents (Figure 14A-B), which revealed crystallization of plagioclase, K-feldspar and amphibole. The negative correlation between La and $(La/Yb)_N$ suggests separation of monazite and/or allanite (Figure 14C).

5.3 Tectonic implications

Zircons analysed from the AK pluton quartz monzonite and monzogranite samples show oscillatory zoning textures in CL images (Figure 5), indicating a magmatic origin (Hoskin and Black 2000). High Th/U ratios (0.4–1.0) are also consistent with them being igneous (Supplementary Table 1; Williams *et al.* 1996). Core–mantle structures were not observed in the CL images (Figure 5); thus, the obtained zircon ages can be assumed to representing the timing of their growth in the melt. The quartz monzonites have crystallization ages between 473 ± 2 Ma and 479 ± 2 Ma, and the monzogranite yielded a weighted mean $^{206}\text{Pb}/^{238}\text{U}$ age of 462 ± 2 Ma. All weighted mean ages were identical within analytical errors to the associated concordant ages. As such, these new data undoubtedly show that the AK pluton was emplaced during the Early Palaeozoic and are consistent with those of the Ordovician arc

magmatism that occurred in the WKOB (Table 1, Figure 1C).

The quartz monzonite and monzogranite from the AK intrusions are enriched in LILEs and LREEs, and depleted in high field strength elements (HFSEs) with negative Nb, Ta, P, Zr, and Ti anomalies in PM normalized trace element patterns, and are similar to other Cambrian–Ordovician arc granitoids in the WKOB (Figure 8B), suggesting they were formed in a subduction environment (Hawkesworth *et al.* 1997; Martin *et al.* 2005). The AK quartz monzonites plotted in the arc field in the La/Sm vs. Sm/Yb diagram and Ta/Yb vs. Yb + Ta diagram (Figure 14D-E; Whalen and Hildebrand 2019), suggesting a subduction setting. Monzogranites have a high silicon content (>68 wt.%) due to the relatively intensive crystalline differentiation, falling into slab failure field. These granitoids had relatively low Rb and Yb + Ta contents and plotted in the volcanic arc granitoids (VAG) field in Rb vs. (Yb + Ta) diagram (Figure 14F; Pearce *et al.* 1984), indicating arc affinities. Therefore, the AK pluton represents an example of Early Palaeozoic arc magmatism in the northern belt of the WKOB.

The WKOB contains numerous Cambrian–Ordovician magmatic rocks, including the 487–532 Ma Nanpingxueshan pluton (Hu *et al.* 2016; Liu *et al.* 2019), 515 Ma Warengzilafu pluton (Zhu *et al.* 2016), 530 Ma Ayilixi pluton (Zhu *et al.* 2016), and 500 Ma Kulule pluton in the MTT (Zhang *et al.* 2016b); the 443–473 Ma Datong complex

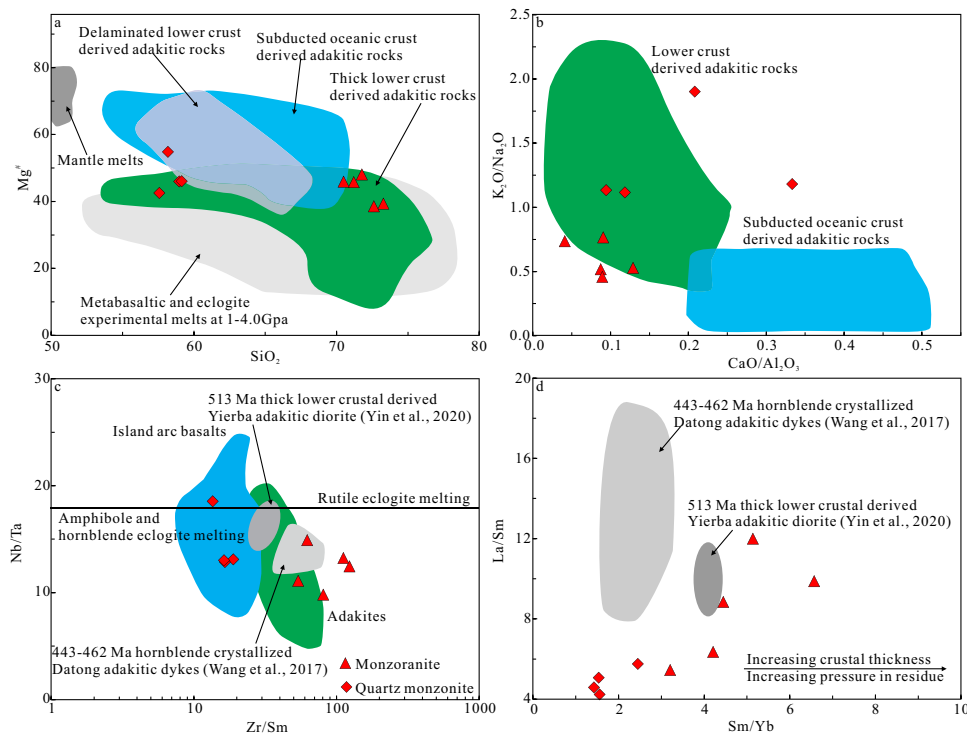


Figure 13. (A) $\text{Mg}^\#$ versus SiO_2 (after Martin *et al.* 2005); (B) $\text{CaO}/\text{Al}_2\text{O}_3$ versus $\text{K}_2\text{O}/\text{Na}_2\text{O}$ (after Karsli *et al.* 2019); (C) Nb/Ta versus Zr/Sm (after Foley *et al.* 2002); (D) La/Sm versus Sm/Yb (after Haschke *et al.* 2006).

(Liao *et al.* 2010; Wang *et al.* 2017; Zhu *et al.* 2018; Li *et al.* 2019), 485 Ma Datongdong pluton (Li *et al.* 2019), 471–513 Ma Yirba pluton (Yuan *et al.* 2002; Liu *et al.* 2014), and 463–479 Ma Akedala pluton in the SKT (This study); and the 502 Ma Dongbake pluton (Cui *et al.* 2007a) and 466 Ma Kashikashi pluton in the NKT (Zhang *et al.* 2019b). Previous studies have shown that these granitoids exhibit similar geochemical characteristics, including variably negative Eu anomalies (Figure 8) and depletion in Nb, Ta, P, and Ti (Figure 8), indicating that they all formed in a subduction zone setting related to the closure of the Proto-Tethys Ocean (Xiao *et al.* 2005; Yuan *et al.* 2005; Cui *et al.* 2007a, b; Liao *et al.* 2010; Liu *et al.* 2014; Hu *et al.* 2016; Wang *et al.* 2017; Zhang *et al.* 2018a; Zhu *et al.* 2018; Li *et al.* 2019; Liu *et al.* 2019; Zhang *et al.* 2019a,b,d; this study). However, the polarity of subduction of the Proto-Tethys Ocean has been debated. Some researchers consider that the Early Palaeozoic Kudi-Qimanyute ophiolite is a remnant of a back-arc basin (Wang *et al.* 2002; Wang 2004), which implies the northward subduction of the Proto-Tethys Ocean (Xiao *et al.* 2000; Wang 2004; Ye *et al.* 2008). In contrast, some researchers interpret it as an ‘supra-subduction zone’ (SSZ) ophiolite, implying that the Proto-Tethys Ocean subducted southward beneath the SKT and MTT (Jiang *et al.* 2002; Liao *et al.* 2010; Jia *et al.* 2013; Liu *et al.* 2014; Li *et al.* 2019; Zhang *et al.* 2018a, p. 2019). In addition, some researchers have reported bidirectional closure of the Proto-Tethys Ocean, indicating the simultaneous operation of subduction zones towards both the north and south (Xiao *et al.* 2002, 2005; Zhu *et al.* 2018).

Examination of the temporal and spatial distribution of the Early Palaeozoic magmatic rocks in the WKOB shows that Cambrian–Ordovician intrusions mostly occur in the SKT and MTT, with minor occurrences in the NKT (Fig. 1C and Table 1). The arc-related pluton in the NKT has an enriched Sr–Nd–Hf isotope composition (Figs. 9–10; Zhang *et al.* 2019d), while the arc magmas in the SKT and MTT have relatively depleted Sr–Nd–Hf isotope compositions (Figs. 9–10; Xiao *et al.* 2005; Yuan *et al.* 2005; Liao *et al.* 2010; Liu *et al.* 2014; Hu *et al.* 2016; Wang *et al.* 2017; Zhang *et al.* 2018a; Zhu *et al.* 2018; Li *et al.* 2019; Liu *et al.* 2019). These characteristics indicate that the arc systems that formed above different subduction zones during closure of the Proto-Tethys Ocean had very different characteristics, with continental arcs characterizing northward subduction beneath the NKT and island arcs characterizing southward subduction beneath the SKT and MTT. These island arcs contain accretionary complexes, volcanic rocks, gabbros, and granites (Zhang *et al.* 2019a). The temporal and spatial distribution of the Early Palaeozoic arc magmas in the WKOB suggests bidirectional subduction of the Proto-Tethys Ocean, with most occurring in a southward direction. As the AK pluton has depleted Sr–Nd–Hf isotopic ratios, it may have formed during the southward subduction of the Proto-Tethys Ocean.

It is generally accepted that the Early Palaeozoic magmatism in the WKOB is related to the tectonic evolution of the Proto-Tethys Ocean (Xiao *et al.* 2005; Yuan *et al.* 2005; Cui *et al.* 2007a, b; Ye *et al.* 2008; Liao *et al.* 2010; Jia

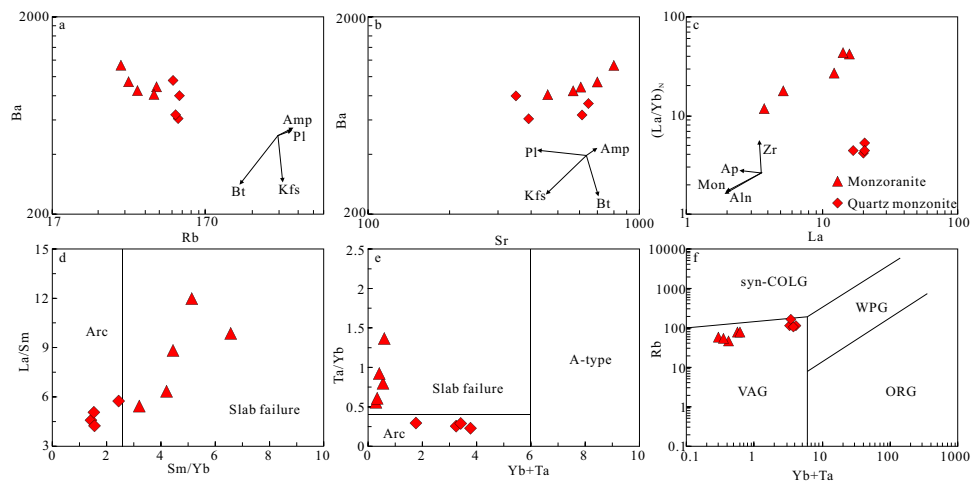


Figure 14. (A) Ba vs. Rb and (B) Ba vs. Sr diagrams showing evidence of fractionation of plagioclase, K-feldspar, and amphibole in the granitoids; (C) $(La/Yb)_N$ vs. La diagram showing crystallization of monzonite and/or allanite; (D) La/Sm vs. Sm/Yb diagrams and (E) Ta/Yb vs. Yb + Ta diagrams (modified after Whalen and Hildebrand 2019) for quartz monzonites and monzogranites from the AK pluton in the WKOB. These data show that the AK quartz monzonites have arc affinities, whereas monzogranites have a high SiO_2 content (>68 wt. %) due to crystalline differentiation, and thus plots in the field for slab failure; (F) Rb vs. (Yb + Ta) diagram (modified after Pearce *et al.* 1984) suggesting a subduction zone setting.

et al. 2013; Liu *et al.* 2014; Hu *et al.* 2016; Wang *et al.* 2017; Zhang *et al.* 2018a; Zhu *et al.* 2018; Li *et al.* 2019; Liu *et al.* 2019; Zhang *et al.* 2019a,b,d); therefore, a comprehensive study of the results from previous studies can be used to decipher the tectonic evolution of the Proto-Tethys Ocean.

The Proto-Tethys Ocean formed between the West Kunlun terrane and Tarim block in the Late Neoproterozoic–Early Palaeozoic (before 530 Ma) during the break-up of the Rodinia supercontinent (Figure 15A; Zhang *et al.* 2004; Metcalfe *et al.* 2017; Zhang *et al.* 2019a). Bidirectional subduction began at 530–500 Ma

(Figure 15B), whereby southward subduction beneath the MTT formed an island arc system accompanied by volcanic rocks, gabbro, and granites that were emplaced into the MTT; meanwhile, northward subduction beneath the NKT formed a continental arc and allowed intrusion of the Dongbake pluton into the NKT at 502 Ma (Cui *et al.* 2007a). This bidirectional subduction continued through 500–460 Ma as the arc systems gradually matured (Figure 15C), forming a large accretionary wedge (SKT) in the fore-arc region. The dehydration of the subducted plate caused partial melting of subducted sediment and partial melting in the overlying mantle

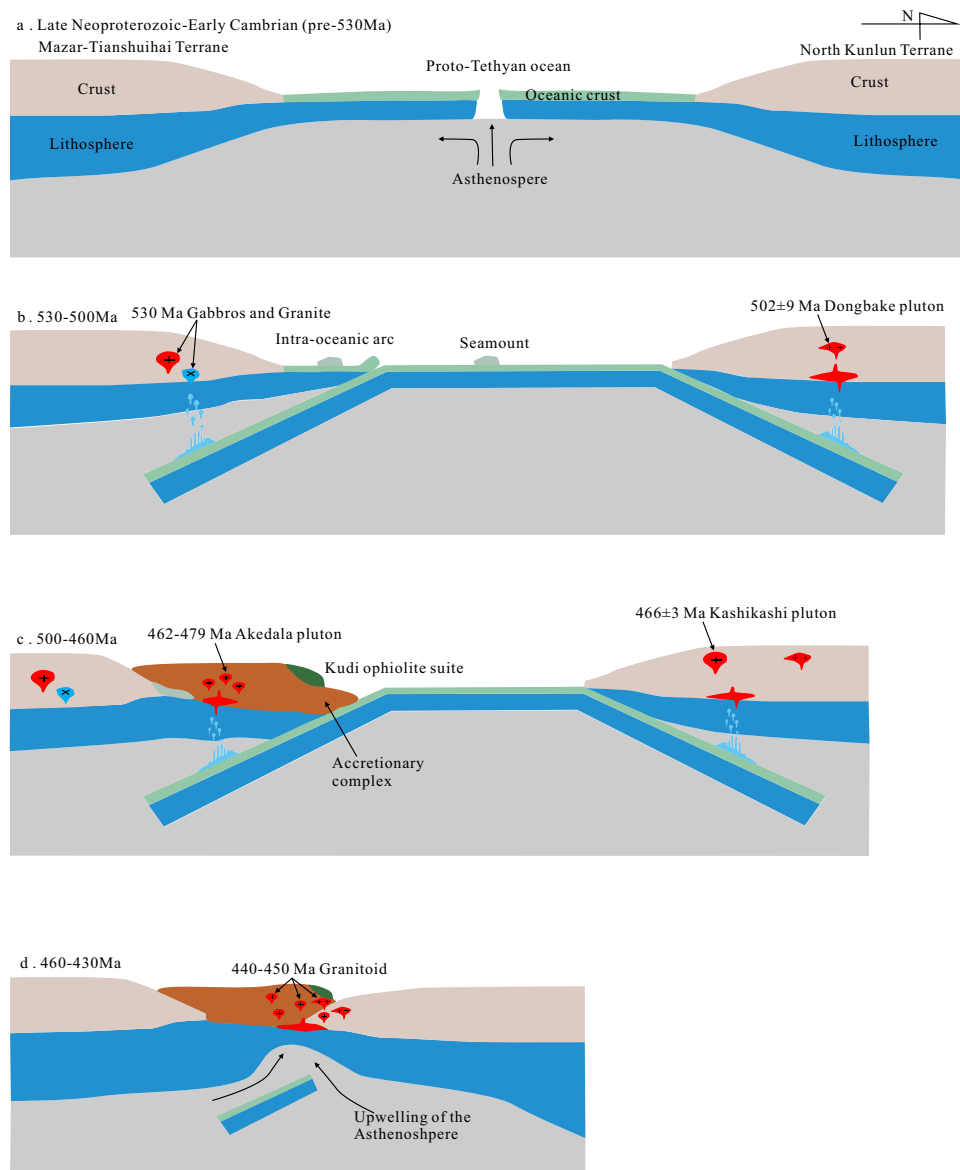


Figure 15. Cartoon illustration showing the tectonic model for generation of the AK pluton. A. Pre-530 Ma: Proto-Tethys Ocean opening between the Tarim block and the MTT. B. 530–500 Ma: bidirectional subduction of the Proto-Tethyan oceanic crust, forming gabbro and granite on both sides. C. 500–460 Ma: continued bidirectional subduction of the Proto-Tethyan oceanic crust, forming the Akedala pluton. D. 460–430 Ma: closure of the Proto-Tethys Ocean, accompanied by collision between the Tarim Block and the West Kunlun terrane, and oceanic slab break-off to form high-K, high-Sr/Y, and high-Ba/Sr granites.

wedge, which led to the formation of bimodal igneous rocks (gabbro and granite) in the SKT (Liu *et al.* 2014; Wang *et al.* 2017; Li *et al.* 2019; Zhang *et al.* 2019a, d; this study) and the intrusion of the Kashikashi pluton in the NKT (Zhang *et al.* 2019b). the closure of the Proto-Tethys Ocean caused a collision between the West Kunlun terrane and the Tarim block at 460–430 Ma, which, in turn, led to metamorphism of volcanic-sedimentary sequences in the accretionary wedge (SKT) under hornblende-bearing granulite-facies conditions at 450–440 Ma (Xiao *et al.* 2005; Wang 2008; Zhang *et al.* 2019a, b). the break-off of the Proto-Tethys oceanic slab and associated asthenospheric upwelling caused emplacement of voluminous high-K, high-Sr/Y and high-Ba/Sr granite into the SKT and NKT (Figure 15D; Ye *et al.* 2008; Jia *et al.* 2013; Zhu *et al.* 2018; Zhang *et al.* 2016d, Zhang *et al.* 2019c).

6. Conclusions

The Akedala pluton is composed of quartz monzonite and monzogranite that were emplaced at 473–479 Ma and 462 Ma, respectively, both of which show geochemical affinities to arc magmas. The depleted whole rock Sr–Nd isotopic ratio ($(^{87}\text{Sr}/^{86}\text{Sr})_i = 0.7042\text{--}0.7058$, $\epsilon_{\text{Nd}}(t) = -0.4$ to $+1.1$), and positive zircon $\epsilon_{\text{Hf}}(t)$ ($+0.0$ to $+6.8$) values of I-type quartz monzonites suggest that they were derived from a mixed source involving juvenile and lower crust. The adakitic monzogranites have depleted whole rock $(^{87}\text{Sr}/^{86}\text{Sr})_i$ (0.7044–0.7045) and positive $\epsilon_{\text{Nd}}(t)$ ($+2.0$ to $+2.9$) and positive zircon $\epsilon_{\text{Hf}}(t)$ ($+1.1$ to $+4.3$) values with low MgO, Cr, Ni, and Nb contents, indicating that they were mainly generated from partial melting of the thickened lower crust. Due to the temporal and spatial distribution of the Early Palaeozoic magmatic rocks in the WKOB, we suggest that bidirectional subduction of the Proto-Tethys Ocean began during the Early Cambrian, and continued to the Middle Ordovician. The Akedala pluton formed due to the southward subduction of the Proto-Tethys Ocean. The final closure of the Proto-Tethys Ocean during the Early Silurian facilitated collision between the Tarim block and the West Kunlun terrane, forming the Early Palaeozoic orogenic belt.

Acknowledgments

This contribution was financially supported by the Natural Science Foundation of China (NSFC Nos. U1603245, 41703051, and U1812402), the Chinese Academy of Sciences “Light of West China” Program, and the Natural Science Foundation of Guizhou Province (No. [2018] 1171). The authors thank Dr. Liang Liu and Dr. Zongyong Yang for his constructive

discussion and guidance that significantly improved the scope of this work. The authors are grateful to Mr. Guangbing Ding and Mr. Hongjun Qin for their assistance during fieldwork. The authors thank Mr. Yanwen Tang for assistance with La–ICM–MS zircon U–Pb analysis, Ms. Shuqing Yang, Ms. Jing Hu, Ms. Yan Huang, and Ms. Fang Xiao for support with whole-rock major and trace element and Sr–Nd isotope measurements, and Mr. Youwei Chen for in situ zircon Hf isotope analysis, and Ms. Shaohua Dong for zircon Cathodoluminescence analysis.

Highlights

- (1) The Akedala pluton is mainly composed of I-type quartz monzonites and adakitic monzogranites that were emplaced at 473–479 Ma and 462 Ma, respectively.
- (2) The granitoids were formed in a subduction zone environment.
- (3) The quartz monzonites were derived from a mixed source of a juvenile mafic crust and an older lower crust.
- (4) The monzogranites were mainly generated from partial melting of thickened lower crust.
- (5) The Akedala pluton was formed during the southward subduction of the Proto-Tethys Ocean.

Disclosure statement

No potential conflict of interest was reported by the authors.

Funding

This work was supported by the Natural Science Foundation of China (NSFC Nos. U1603245, 41703051, and U1812402), the Chinese Academy of Sciences “Light of West China” Program, the Natural Science Foundation of Guizhou Province (No. [2018] 1171), and the frontier project of the State Key Laboratory of Ore Deposit Geochemistry, Institute of Geochemistry, Chinese Academy of Sciences.

References

- Belliemi, G., Comin-Chiaromonti, P., Marques, L.S., Melfi, A.J., Nardy, A., Papatrechas, C., Piccirillo, E.M., Roisenberg, A., and Stolfa, D. 1986. Petrogenetic aspects of acid and basaltic lavas from the Paraná plateau (Brazil): Geological, mineralogical and petrochemical relationships: *Journal of Petrology*, 27, 915–944. [10.1093/petrology/27.4.915](https://doi.org/10.1093/petrology/27.4.915). 4.
- Chappell, B.W., and White, A.J.R. 1992. I- and S-type granites in the Lachlan Fold Belt: Earth and Environmental Science Transactions of the Royal Society of Edinburgh, 83, 1–26. [10.1017/S0263593300007720](https://doi.org/10.1017/S0263593300007720). 1–2.
- Chauvel, C., and Blichert-Toft, J. 2001. A hafnium isotope and trace element perspective on melting of the depleted mantle: *Earth and Planetary Science Letters*, 190, 137–151. [10.1016/S0012-821X\(01\)00379-X](https://doi.org/10.1016/S0012-821X(01)00379-X). 3–4.
- Chauvel, C., Lewin, E., Carpentier, M., Arndt, N.T., and Marini, J. C. 2008. Role of recycled oceanic basalt and sediment in generating the Hf–Nd mantle array: *Nature Geoscience*, 1, 64–67. [10.1038/ngeo.2007.51](https://doi.org/10.1038/ngeo.2007.51). 1.

- Chauvel, C., Marini, J., Plank, T., and Ludden, J. 2009. Hf-Nd input flux in the Izu-Mariana subduction zone and recycling of subducted material in the mantle: *Geochemistry Geophysics Geosystems*, 10, 1–23. [10.1029/2008GC002101](https://doi.org/10.1029/2008GC002101). 1.
- Chung, S.L., Liu, D.Y., Ji, J.Q., Chu, M.F., Lee, H.Y., Wen, D.J., Lo, C. H., Lee, T.Y., Qian, Q., and Zhang, Q. 2003. Adakites from continental collision zones: Melting of thickened lower crust beneath southern Tibet: *Geology*, 31, 1021–1024. [10.1130/G19796.1](https://doi.org/10.1130/G19796.1). 11.
- Collins, W.J., Beams, S.D., White, A.J.R., and Chappell, B.W. 1982. Nature and origin of A-type granites with particular reference to southeastern Australia: Contributions to mineralogy and petrology, 80. 189–200. <https://doi.org/10.1007/BF00374895>
- Cui, J.T., Wang, J.C., Bian, X.W., Luo, Q.Z., Zhu, H.P., Wang, M.C., and Chen, G.C. 2007b. Zircon SHRIMP U-Pb dating of the Dongbake gneissic tonalite in northern Kangxiwar, West Kunlun: *Geological Bulletin of China*, 26, 726–729. [10.1016/S1872-5791\(07\)60044-X](https://doi.org/10.1016/S1872-5791(07)60044-X).
- Cui, J.T., Wang, J.C., Bian, X.W., Zhu, H.P., Luo, Q.Z., Yang, K.J., and Wang, M.C. 2007a. Zircon SHRIMP U-Pb dating of early Paleozoic granite in the Menggubao-Pushou area on the northern side of Kangxiwar, West Kunlun: *Geological Bulletin of China*, 26, 710–719. in Chinese with English abstract. [10.3969/j.1671-2552.2007.06.012](https://doi.org/10.3969/j.1671-2552.2007.06.012).
- Cui, J.T., Wang, J.C., Bian, X.W., Zhu, H.P., and Yang, K.J. 2006. Geological characteristics of early Paleozoic amphibolite and tonalite in northern Kangxiwar, West Kunlun, China and their zircon SHRIMP U-Pb dating: *Geological Bulletin of China*, 25, 1441–1449. in Chinese with English abstract.
- Defant, M.J., and Drummond, M.S. 1990. Derivation of some modern arc magmas by melting of young subducted lithosphere: *Nature*, 347, 662–665. [10.1038/347662a0](https://doi.org/10.1038/347662a0). 6294.
- Foley, S., Tiepolo, M., and Vannucci, R. 2002. Growth of early continental crust controlled by melting of amphibolite in subduction zones: *Nature*, 417, 837–840. [10.1038/nature00799](https://doi.org/10.1038/nature00799). 6891.
- Garland, F., Hawkesworth, C.J., and Mantovani, M.S.M. 1995. Description and petrogenesis of the Paraná Rhyolites, Southern Brazil: *Journal of Petrology*, 36, 1193–1227. [10.1093/petrology/36.5.1193](https://doi.org/10.1093/petrology/36.5.1193). 5.
- Griffin, W.L., Wang, X., Jackson, S.E., Pearson, N.J., O'Reilly, S.Y., Xu, X., and Zhou, X. 2002. Zircon chemistry and magma mixing, SE China: In-situ analysis of Hf isotopes, Tonglu and Pingtan igneous complexes: *Lithos*, 61, 237–269. [10.1016/S0024-4937\(02\)00082-8](https://doi.org/10.1016/S0024-4937(02)00082-8). 3–4.
- Haschke, M., Günther, A., Melnick, D., Ehtler, H., Reutter, K.J., Scheuber, E., and Oncken, O., 2006. Central and southern andean tectonic evolution inferred from arc magmatism, pp. 337–353. doi: [10.1007/978-3-540-48684-8_16](https://doi.org/10.1007/978-3-540-48684-8_16)
- Hawkesworth, C.J., Turner, S., Mcdermott, F., Peate, D.W., and Van Calsteren, P. 1997. U-Th isotopes in arc magmas: Implications for Element Transfer from the Subducted Crust: *Science*, 276, 551–555. [10.1126/science.276.5312.551](https://doi.org/10.1126/science.276.5312.551). 5312.
- Henan Institute of Geological Survey, 2005, Geological survey report for 1:250,000 of Yingjisha County: 1–392 (in Chinese).
- Hoskin, P.W.O., and Black, L.P. 2000. Metamorphic zircon formation by solid-state recrystallization of protolith igneous zircon: *Journal of Metamorphic Geology*, 18, 423–439. [10.1046/j.1525-1314.2000.00266.x](https://doi.org/10.1046/j.1525-1314.2000.00266.x). 4.
- Hu, J., Wang, H., Huang, C., Tong, L., Mu, S., and Qiu, Z. 2016. Geological characteristics and age of the dahongliutan fe-ore deposit in the western kunlun orogenic belt, xinjiang, northwestern china: *Journal of Asian Earth Sciences*, 116, 1–25. [10.1016/j.jseaes.2015.08.014](https://doi.org/10.1016/j.jseaes.2015.08.014).
- Hu, J., Wang, H., Mu, S.L., and Wang, M. 2017a. Geochemistry and Hf isotopic compositions of early Paleozoic granites in Nanpingxueshan from the Tianshuihai terrane, west Kunlun: Crust-mantle magmatism: *Acta Geologica Sinica*, 91, 1192–1207. in Chinese with English abstract.
- Hu, X.Y. 2018. Petrogenesis and Tectonic Significance of granitic pluton and MMEs in the eastern segment of the Tielike. NW China: Xinjiang University. Master thesis. 1–69. in Chinese with English abstract.
- Hu, X.Y., Guo, R.Q., Nuerkanati-Madayipu,, Guo, Y., Zhou, M.Y., and Lv., B. 2017b. Zircon U-Pb dating, petrology, geochemistry of the buya pluton and its mmes in the southern margin of tarim: *Rock and Mineral Analysis*, 36, 538–550. in Chinese with English abstract.
- Ji, W., Li, R., Chen, S., He, S., Zhao, Z., Bian, X., and Ren, J. 2011. The discovery of palaeoproterozoic volcanic rocks in the bulunkuoler group from the tianshuihai massif in Xinjiang of northwest China and its geological significance: *Science China Earth Sciences*, 54, 61–72. [10.1007/s11430-010-4043-7](https://doi.org/10.1007/s11430-010-4043-7). 1.
- Ji, W.H., Chen, S.J., Li, R.S., He, S.P., Zhao, Z.M., and Pan, X.P. 2018. The origin of Carboniferous-Permian magmatic rocks in Oytage area, West Kunlun: Back-arc basin?: *Acta Petrologica Sinica*, 34, 2393–2409. in Chinese with English abstract.
- Jia, R.Y., Jiang, Y.H., Liu, Z., Zhao, P., and Zhou, Q. 2013. Petrogenesis and tectonic implications of early Silurian high-K calc-alkaline granites and their potassic microgranular enclaves, western Kunlun orogen, NW tibetan plateau: *International Geology Review*, 55, 958–975. [10.1080/00206814.2012.755766](https://doi.org/10.1080/00206814.2012.755766). 8.
- Jiang, Y.H., Jiang, S.Y., Ling, H.F., Zhou, X.R., Rui, X.J., and Yang, W.Z. 2002. Petrology and geochemistry of shoshonitic plutons from the western Kunlun orogenic belt, northwestern Xinjiang, China: Implications for granitoid geneses: *Lithos*, 63, 165–187. [10.1016/S0024-4937\(02\)00140-8](https://doi.org/10.1016/S0024-4937(02)00140-8). 3–4.
- Jiang, Y.H., Liao, S.Y., Yang, W.Z., and Shen, W.Z. 2008. An island arc origin of plagiogranites at Oytage, western Kunlun orogen, northwest China: SHRIMP zircon U-Pb chronology, elemental and Sr-Nd-Hf isotopic geochemistry and Paleozoic tectonic implications: *Lithos*, 106, 323–335. [10.1016/j.lithos.2008.08.004](https://doi.org/10.1016/j.lithos.2008.08.004). 3–4.
- Karsli, O., Dokuz, A., Kandemir, R., Aydin, F., Schmitt, A.K., and Yalçin, E.E. 2019. Adakite-like parental melt generation by partial fusion of juvenile lower crust, Sakarya zone, NE Turkey: A far-field response to break-off of the southern Neotethyan oceanic lithosphere: *Lithos*, 338–339, 58–72. [10.1016/j.lithos.2019.03.029](https://doi.org/10.1016/j.lithos.2019.03.029).
- Li, Y., Xiao, W., and Tian, Z. 2019. Early Palaeozoic accretionary tectonics of west kunlun orogen: insights from datong granitoids, mafic-ultramafic complexes, and silurian-devonian sandstones, Xinjiang, NW China: *Geological Journal*, 54, 1505–1517. [10.1002/gj.3246](https://doi.org/10.1002/gj.3246). 3.
- Liao, S.Y., Jiang, Y.H., Jiang, S.Y., Yang, W.Z., Zhou, Q., Jin, G.D., and Zhao, P. 2010. Subducting sediment-derived arc granitoids: Evidence from the Datong pluton and its quenched enclaves in the western Kunlun orogen, northwest China: *Mineralogy and Petrology*, 100, 55–74. [10.1007/s00710-010-0122-x](https://doi.org/10.1007/s00710-010-0122-x). 1–2.

- Liu, X., Zhu, Z.X., Guo, R.Q., Zhu, Y.F., Li, P., and Jin, L.Y. 2016. LA-ICP-MS zircon U-Pb dating and its geological significance for Late Paleozoic diabase from the west part of Tiekelike area, south Tarim: *Geological Sciences*, 3, 794–805. in Chinese with English abstract. [10.12017/dzlx.2016.030](https://doi.org/10.12017/dzlx.2016.030).
- Liu, X.Q., Zhang, C.L., Ye, X.T., Zou, H., and Hao, X.S. 2019. Cambrian mafic and granitic intrusions in the Mazar-Tianshuihai terrane, west kunlun orogenic belt: constraints on the subduction orientation of the proto-tethys ocean: *Lithos*, 350, [10.1016/j.lithos.2019.105226](https://doi.org/10.1016/j.lithos.2019.105226).
- Liu, Y.S., Hu, Z.C., Gao, S., Günther, D., Xu, J., Gao, C.G., and Chen, H.H. 2008. In situ analysis of major and trace elements of anhydrous minerals by LA-ICP-MS without applying an internal standard: *Chemical Geology*, 257, 34–43. [10.1016/j.chemgeo.2008.08.004](https://doi.org/10.1016/j.chemgeo.2008.08.004). 1–2.
- Liu, Y.S., Hu, Z.C., Zong, K.Q., Gao, C.G., Gao, S., Xu, J., and Chen, H.H. 2010. Re-appraisal and refinement of zircon U-Pb isotope and trace element analyses by LA-ICP-MS: *Chinese Science Bulletin*, 55, 1535–1546. [10.1007/s11434-010-3052-4](https://doi.org/10.1007/s11434-010-3052-4). 15.
- Liu, Z., Jiang, Y.H., Jia, R.Y., Zhao, P., Zhou, Q., Wang, G.C., and Ni, C.Y. 2014. Origin of Middle Cambrian and Late Silurian potassic granitoids from the western Kunlun orogen, north-west China: A magmatic response to the Proto-Tethys evolution: *Mineralogy and Petrology*, 108, 91–110. [10.1007/s00710-013-0288-0](https://doi.org/10.1007/s00710-013-0288-0). 1.
- Ludwig, K.R. 2003. User's Manual for Isoplot 3.00, a geochronological Toolkit for Microsoft Excel: Berkeley Geochronological Center Special Publication, 4, 25–32.
- Macpherson, C.G., Dreher, S.T., and Thirwall, M.F. 2006. Adakites without slab melting: High pressure processing of basaltic island arc magma, Mindanao, the Philippines: *Earth and Planetary Science Letters*, 243, 581–593. [10.1016/j.epsl.2005.12.034](https://doi.org/10.1016/j.epsl.2005.12.034). 3–4.
- Maniar, P.D., and Piccoli, P.M. 1989. Tectonic discrimination of granitoids: *Geological Society of America Bulletin*, 101, 635–643. [10.1130/0016-7606\(1989\)101<0635:TDOG>2.3.CO;2](https://doi.org/10.1130/0016-7606(1989)101<0635:TDOG>2.3.CO;2). 5.
- Martin, H. 1999. Adakitic magmas modern analogues of Archaean granitoids: *Lithos*, 46, 411–429. [10.1016/S0024-4937\(98\)00076-0](https://doi.org/10.1016/S0024-4937(98)00076-0). 3.
- Martin, H., Smithies, R.H., Rapp, R., Moyen, J.F., and Champion, D. 2005. An overview of adakite, tonalite-trondhjemite-granodiorite (TTG), and sanukitoid: Relationships and some implications for crustal evolution: *Lithos*, 79, 1–24. [10.1016/j.lithos.2004.04.048](https://doi.org/10.1016/j.lithos.2004.04.048). 1–2.
- Metcalf, I., Henderson, C.M., and Wakita, K. 2017. Lower permian conodonts from palaeo-tethys ocean plate stratigraphy in the Chiang Mai-Chiang Rai suture zone, northern Thailand: *Gondwana Research*, 44, 54–66. [10.1016/j.gr.2016.12.003](https://doi.org/10.1016/j.gr.2016.12.003).
- Middlemost, E.A. 1994. Naming materials in the magma/igneous rock system: *Earth-Science Reviews*, 37, 215–224. [10.1016/0012-8252\(94\)90029-9](https://doi.org/10.1016/0012-8252(94)90029-9). 3–4.
- Pan, Y.S. 2000. Geological evolution of the Karakorum and Kunlun mountains. Science Press: Beijing, 1–539. in Chinese with English abstract.
- Pearce, J.A., Harris, N.B., and Tindle, A.G. 1984. Trace element discrimination diagrams for the tectonic interpretation of granitic rocks: *Journal of Petrology*, 25, 956–983. [10.1093/ptrology/25.4.956](https://doi.org/10.1093/ptrology/25.4.956). 4.
- Qi, L., Jing, H., and Gregoire, D.C. 2000. Determination of trace elements in granites by inductively coupled plasma mass spectrometry: *Talanta*, 51, 507–513. [10.1016/S0039-9140\(99\)00318-5](https://doi.org/10.1016/S0039-9140(99)00318-5). 3.
- Rapp, R.P., Shimizu, N., Norman, M.D., and Applegate, G.S. 1999. Reaction between slab-derived melts and peridotite in the mantle wedge: Experimental constraints at 3.8 GPa: *Chemical Geology*, 160, 335–356. [10.1016/S0009-2541\(99\)00106-0](https://doi.org/10.1016/S0009-2541(99)00106-0). 4.
- Rapp, R.P., and Watson, E.B. 1995. Dehydration melting of metabasalt at 8–32 kbar: Implications for continental growth and crust-mantle recycling: *Journal of Petrology*, 36, 891–931. [10.1093/ptrology/36.4.891](https://doi.org/10.1093/ptrology/36.4.891). 4.
- Richards, J.P., and Kerrich, R. 2007. Special paper adakite-like rocks their diverse origins and questionable role in metallogenesis: *Economic Geology*, 102, 537–576. [10.2113/gsecongeo.102.4.537](https://doi.org/10.2113/gsecongeo.102.4.537). 4.
- Rudnick, R.L., and Gao, S. 2003. The composition of the continental crust. Rudnick, R.L., ed., *The Crust*. Elsevier-Pergamon, Oxford. 1–64. [10.1016/B0-08-043751-6/03016-4](https://doi.org/10.1016/B0-08-043751-6/03016-4).
- Stern, C.R., and Kilian, R. 1996. Role of the subducted slab, mantle wedge and continental crust in the generation of adakites from the Austral Volcanic Zone: *Contributions to Mineralogy and Petrology*, 123, 263–281. [doi:10.1007/s004100050155](https://doi.org/10.1007/s004100050155)
- Streck, M.J., Leeman, P.W., and Chesley, J. 2007. Highmagnesian andesite from Mount Shasta: A product of magma mixing and contamination, not a primitive mantle melt: *Geology*, 35, 351–354. [10.1130/G23286A.1](https://doi.org/10.1130/G23286A.1). 4.
- Streckeisen, A. 1967. Classification and nomenclature of igneous rocks: *Neues Jahrbuch Für Mineralogie - Abhandlungen*, 107, 144–204.
- Sun, S.S., and McDonough, W.F. 1989. Chemical and isotopic systematics of oceanic basalts: Implications for mantle composition and processes: *Geological Society, London, Special Publications*, 42, 313–345. [10.1144/GSL.SP.1989.042.01.19](https://doi.org/10.1144/GSL.SP.1989.042.01.19). 1.
- Wang, C., Liu, L., He, S.P., Yang, W.Q., Cao, Y.T., and Zhu, X.H. 2013. Early Paleozoic magmatism in west Kunlun: Constraints from geochemical and zircon U-Pb-Hf isotope studies of the Bulong granite: *Chinese Journal of Geology*, 48, 997–1014. in Chinese with English abstract.
- Wang, J., Hattori, K., Liu, J., Song, Y., Gao, Y., and Zhang, H. 2017. Shoshonitic and adakitic magmatism of the early Paleozoic age in the western Kunlun orogenic belt, NW China: implications for the early evolution of the northwestern Tibetan plateau: *Lithos*, 286, 345–362. [10.1016/j.lithos.2017.06.013](https://doi.org/10.1016/j.lithos.2017.06.013).
- Wang, J.P. 2008. Geological features and tectonic significance of melange zone in the Taxkorgan area, West Kunlun: *Geological Bulletin of China*, 27, 2057–2066. in Chinese with English abstract.
- Wang, Q., Xu, J.F., Jian, P., Bao, Z.W., Zhao, Z.H., Li, C.F., Xiong, X.L., and Ma, J.L. 2006. Petrogenesis of adakitic porphyries in an extensional tectonic setting, Dexing, South China: implications for the genesis of porphyry copper mineralization: *Journal of Petrology*, 47, 119–144. [10.1093/ptrology/egi070](https://doi.org/10.1093/ptrology/egi070). 1.
- Wang, Z., Sun, S., Li, J., and Hou, Q. 2002. Petrogenesis of tholeiite associations in Kudi ophiolite, western Kunlun mountains, northwestern China: Implications for the

- evolution of back-arc basins: Contributions to Mineralogy and Petrology, 143, 471–483. [10.1007/s00410-002-0358-5](https://doi.org/10.1007/s00410-002-0358-5). 4.
- Wang, Z.H. 2004. Tectonic evolution of the western Kunlun orogenic belt, western China: Journal of Asian Earth Sciences, 24, 153–161. [10.1016/j.jseaes.2003.10.007](https://doi.org/10.1016/j.jseaes.2003.10.007). 2.
- Whalen, J.B., Currie, K.L., and Chappell, B.W. 1987. A-type granites: geochemical characteristics, discrimination and petrogenesis: Contributions to Mineralogy and Petrology, 95, 407–419. <https://doi.org/10.1007/BF00402202>
- Whalen, J.B., and Hildebrand, R. 2019. Trace element discrimination of arc, slab failure, and A-type granitic rocks: Lithos, 348–349, Paper number. 105179.
- Williams, I.S., Buick, I.S., and Cartwright, I. 1996. An extended episode of early Mesoproterozoic metamorphic fluid flow in the Reynolds range, central Australia: Journal of Metamorphic Geology, 14, 29–47. [10.1111/j.1525-1314.1996.00029.x](https://doi.org/10.1111/j.1525-1314.1996.00029.x). 1.
- Wu, F.Y., Jahn, B.M., Wilde, S.A., Lo, C.H., Yui, T.F., Lin, Q., and Sun, D.Y. 2003. Highly fractionated I-type granites in NE China (I): Geochronology and petrogenesis: Lithos, 66, 241–273. [10.1016/S0024-4937\(02\)00222-0](https://doi.org/10.1016/S0024-4937(02)00222-0). 3–4.
- Xiao, W., Hou, Q., Li, J., Hao, J., Fang, A., Zhou, H., and Yuan, C. 2000. Tectonic facies and the archipelago-accretion process of the west Kunlun, China: Science in China Series D: Earth Sciences, 43, 134–143. [10.1007/BF02911939](https://doi.org/10.1007/BF02911939).
- Xiao, W.J., Windley, B.F., Chen, H.L., Zhang, G.C., and Li, J.L. 2002. Carboniferous-Triassic subduction and accretion in the western Kunlun, China: Implications for the collisional and accretionary tectonics of the northern Tibetan Plateau: Geology, 30, 295–298. [10.1130/0091-7613\(2002\)030<0295:CTSAAL>2.0.CO;2](https://doi.org/10.1130/0091-7613(2002)030<0295:CTSAAL>2.0.CO;2). 4.
- Xiao, W.J., Windley, B.F., Liu, D.Y., Jian, P., Liu, C.Z., Yuan, C., and Sun, M. 2005. Accretionary tectonics of the western Kunlun orogen, China: A Paleozoic-early Mesozoic, long lived active continental margin with implications for the growth of southern Eurasia: The Journal of Geology, 113, 687–705. [10.1086/449326](https://doi.org/10.1086/449326). 6.
- Ye, H.M., Li, X.H., Li, Z.X., and Zhang, C.L. 2008. Age and origin of high Ba–Sr apatite–granites at the northwestern margin of the Tibet Plateau: Implications for early Paleozoic tectonic evolution of the Western Kunlun orogenic belt: Gondwana Research, 13, 126–138. [10.1016/j.gr.2007.08.005](https://doi.org/10.1016/j.gr.2007.08.005). 1.
- Ye, X.T., Zhang, C.L., Santosh, M., Zhang, J., Fan, X.K., and Zhang, J.J. 2016. Growth and evolution of Precambrian continental crust in the southwestern Tarim terrane: New evidence from the ca. 1.4 Ga A-type granites and Paleoproterozoic intrusive complex: Precambrian Research, 275, 18–34. [10.1016/j.precamres.2015.12.017](https://doi.org/10.1016/j.precamres.2015.12.017).
- Yin, J., Xiao, W., Sun, M., Chen, W., Yuan, C., Zhang, Y., and Xia, X. 2020. Petrogenesis of Early Cambrian granitoids in the western Kunlun orogenic belt, Northwest Tibet: Insight into early stage subduction of the Proto-Tethys Ocean. GSA Bulletin: in press. [10.1130/B35408.1](https://doi.org/10.1130/B35408.1).
- Yuan, C., Sun, M., Zhou, M.F., Xiao, W.J., and Zhou, H. 2005. Geochemistry and petrogenesis of the Yishak volcanic sequence, Kudi ophiolite, West Kunlun (NW China): Implications for the magmatic evolution in a subduction zone environment: Contributions to Mineralogy and Petrology, 150, 195–211. [10.1007/s00410-005-0012-0](https://doi.org/10.1007/s00410-005-0012-0). 2.
- Yuan, C., Sun, M., Zhou, M.F., Zhou, H., Xiao, W.J., and Li, J.L. 2002. Tectonic evolution of the West Kunlun: Geochronologic and geochemical constraints from Kudi Granitoids: International Geology Review, 44, 653–669. [10.2747/0020-6814.44.7.653](https://doi.org/10.2747/0020-6814.44.7.653). 7.
- Zhang, C., Yu, H., Ye, H., Zhao, Y., and Zhang, D. 2006. Aoyitake plagiogranite in western Tarim Block, NW China: Age, geochemistry, petrogenesis and its tectonic implications: Science in China Series D: Earth Sciences, 49, 1121–1134. [10.1007/s11430-006-1121-y](https://doi.org/10.1007/s11430-006-1121-y).
- Zhang, C.L., Li, Z.X., Li, X.H., Yu, H.F., and Ye, H.M. 2007a. An early Paleoproterozoic high-K intrusive complex in southwestern Tarim Block, NW China: Age, geochemistry, and tectonic implications: Gondwana Research, 12, 101–112. [10.1016/j.gr.2006.10.006](https://doi.org/10.1016/j.gr.2006.10.006). 1–2.
- Zhang, C.L., Ma, D.H., Zhu, B.Y., Ye, X.T., Qiu, L., Zhao, H.X., Liu, X.Q., Ding, T., Wang, Q., and Hao, X.S. 2019a. Tectonic evolution of the Western Kunlun-Karakorum Orogenic Belt and its coupling with the mineralization effect: Geological Review, 65, 1077–1102. in Chinese with English abstract.
- Zhang, C.L., Ye, X.T., Zou, H.B., and Chen, X.Y. 2016a. Neoproterozoic sedimentary basin evolution in southwestern Tarim, NW China: New evidence from field observations, detrital zircon U–Pb ages and Hf isotope compositions: Precambrian Research, 280, 31–45. [10.1016/j.precamres.2016.04.011](https://doi.org/10.1016/j.precamres.2016.04.011).
- Zhang, C.L., Yu, H.F., Shen, J.L., Dong, Y.G., Ye, H.M., and Guo, K.Y. 2004. Zircon SHRIMP age determination of the giant-crystal gabbro and basalt in Kuda, west Kunlun: Dismembering of the Kuda Ophiolite: Geological Review, 50, 639–650. in Chinese with English abstract.
- Zhang, C.L., Zou, H.B., Ye, X.T., and Chen, X.Y. 2018a. Timing of subduction initiation in the Proto-Tethys Ocean: Evidence from the Cambrian gabbros from the NE Pamir Plateau: Lithos, 314, 40–51. [10.1016/j.lithos.2018.05.021](https://doi.org/10.1016/j.lithos.2018.05.021).
- Zhang, C.L., Zou, H.B., Ye, X.T., and Chen, X.Y. 2018b. Tectonic evolution of the NE section of the Pamir Plateau: New evidence from field observations and zircon U–Pb geochronology: Tectonophysics, 723, 27–40. [10.1016/j.tecto.2017.11.036](https://doi.org/10.1016/j.tecto.2017.11.036).
- Zhang, C.L., Zou, H.B., Ye, X.T., and Chen, X.Y. 2018c. A newly identified Precambrian terrane at the Pamir Plateau: The Archean basement and Neoproterozoic granitic intrusions: Precambrian Research, 304, 73–87. [10.1016/j.precamres.2017.11.006](https://doi.org/10.1016/j.precamres.2017.11.006).
- Zhang, C.L., Zou, H.B., Ye, X.T., and Chen, X.Y. 2019b. Tectonic evolution of the West Kunlun Orogenic Belt along the northern margin of the Tibetan Plateau: Implications for the assembly of the Tarim terrane to Gondwana: Geoscience Frontiers, 10, 973–988. [10.1016/j.gsf.2018.05.006](https://doi.org/10.1016/j.gsf.2018.05.006). 3.
- Zhang, H.S., He, S.P., Ji, W.H., Wang, C., Shi, J.B., Kang, K.Y., and Xi, D.H. 2016b. Implications of late Cambrian granite in Tianshuihai massif for the evolution of proto tethys ocean: Evidences from zircon geochronology and geochemistry: Acta Geologica Sinica, 90, 2582–2602. in Chinese with English abstract.
- Zhang, Q., Liu, Y., Huang, H., Wu, Z., and Zhou, Q. 2016d. Petrogenesis and tectonic implications of the high-K Alamas calc-alkaline granitoids at the northwestern margin of the Tibetan Plateau: Geochemical and Sr–Nd–Hf–O isotope constraints: Journal of Asian Earth Sciences, 127, 137–151. [10.1016/j.jseaes.2016.05.026](https://doi.org/10.1016/j.jseaes.2016.05.026).
- Zhang, Q., Wu, Z., Chen, X., Zhou, Q., and Shen, N. 2019c. Proto-Tethys oceanic slab break-off: Insights from early

- Paleozoic magmatic diversity in the West Kunlun Orogen, NW Tibetan Plateau: *Lithos*, 346, 105147. [10.1016/j.lithos.2019.07.014](https://doi.org/10.1016/j.lithos.2019.07.014).
- Zhang, Q., Wu, Z.H., Li, S., Li, K., Liu, Z.W., and Zhou, Q. 2019d. Ordovician granitoids and silurian mafic dikes in the western kunlun orogen, Northwest China: implications for evolution of the proto-tethys: *Acta Geologica Sinica-english Edition*, 93, 30–49. [10.1111/1755-6724.13760](https://doi.org/10.1111/1755-6724.13760). 1.
- Zhang, Y., Niu, Y., Hu, Y., Liu, J., Ye, L., Kong, J., and Duan, M. 2016c. The syncollisional granitoid magmatism and continental crust growth in the West Kunlun Orogen, China-Evidence from geochronology and geochemistry of the Arkarz pluton: *Lithos*, 245, 191–204. [10.1016/j.lithos.2015.05.007](https://doi.org/10.1016/j.lithos.2015.05.007).
- Zhang, Z.W., Cui, J.T., Wang, J.C., Bian, X.W., Zhu, H.P., Luo, Q.Z., and Wang, M.C. 2007b. SHRIMP U-Pb dating of Early Paleozoic amphibolite and granodiorite in Korliang, northwestern Kangxiwa, West Kunlun: *Geological Bulletin*, 26, 720–725. in Chinese with English abstract.
- Zhang, Z.W., Shen, N.P., Peng, J.T., Yang, X.Y., Feng, G., Yu, F., Zhou, L.J., Li, Y.J., and Wu, C.Q. 2014. Syndeposition and epigenetic modification of the strata-bound Pb-Zn-Cu deposits associated with carbonate rocks in western Kunlun, Xinjiang, China: *Ore Geology Reviews*, 62, 227–244. [10.1016/j.oregeorev.2014.04.001](https://doi.org/10.1016/j.oregeorev.2014.04.001).
- Zhang, Z.W., Wu, C.Q., Zhu, W.G., Luo, T.Y., Xu, J.H., Hu, P.C., Li, X.Y., and Jin, Z.R., 2019e, The Late Palaeozoic Back-arc Basin and metallogenesis in West Kunlun: The Ninth National Symposium on Mineralization Theory and Prospecting Methods, 444–445 (in Chinese).
- Zheng, Y.Z., Yang, W.W., and Wang, T. 2013. Geochemistry and geological significance of intrusive rocks of early Paleozoic in Western Kunlun, Xinjiang: *Northwestern Geology*, 4, 57–65. in Chinese with English abstract. [10.3969/j.1009-6248.2013.04.006](https://doi.org/10.3969/j.1009-6248.2013.04.006).
- Zhu, D.C., Mo, X.X., Niu, Y.L., Zhao, Z.D., Wang, L.Q., Liu, Y.S., and Wu, F.Y. 2009. Geochemical investigation of Early Cretaceous igneous rocks along an east-west traverse throughout the central Lhasa Terrane, Tibet: *Chemical Geology*, 268, 298–312. [10.1016/j.chemgeo.2009.09.008](https://doi.org/10.1016/j.chemgeo.2009.09.008). 3–4.
- Zhu, J., Li, Q., Chen, X., Tang, H., Wang, Z., Chen, Y., and Chen, J. 2018. Geochemistry and petrogenesis of the early Palaeozoic appinite-granite complex in the western kunlun orogenic belt, NW China: Implications for Palaeozoic tectonic evolution: *Geological Magazine*, 155, 1641–1666. [10.1017/S0016756817000450](https://doi.org/10.1017/S0016756817000450). 8.
- Zhu, J., Li, Q.G., Wang, Z.Q., Tang, H.S., Chen, X., and Xiao, B. 2016. Magmatism and tectonic implication of early Cambrian granitoid plutons in Tianshuhai Terrane of the western kunlun orogenic belt, northwest China: *Northwestern Geology*, 49, 1–18. in Chinese with English abstract.
- Zhuan, S.P., Bai, C.D., Mao, Z.F., Li, D., Zhang, X.Z., Chen, Y. Y., and Lian, Q. 2018. Zircon U-Pb age and geochemical characteristics of the Sugatlik late Silurian granites in southern Kudi, Xinjiang and its geotectonic significance: *Journal of Geomechanics*, 24, 79–87. in Chinese with English abstract.